POLITECNICO DI TORINO
Repository ISTITUZIONALE

Three-dimensional pollutant dispersion in tree-lined urban canyons: Combined wind-tunnel and LES analysis

Original
Three-dimensional pollutant dispersion in tree-lined urban canyons: Combined wind-tunnel and LES analysis / Fellini, S., Majumdar, D., Salizzoni, P., Van Reeuwijk, M.. - In: ATMOSPHERIC ENVIRONMENT. - ISSN 1352-2310. - 367:(2026). [10.1016/j.atmosenv.2025.121748]

Availability:
This version is available at: 11583/3007651 since: 2026-02-16T07:56:13Z

Publisher:
Elsevier

Published
DOI:10.1016/j.atmosenv.2025.121748

Terms of use:

This article is made available under terms and conditions as specified in the corresponding bibliographic description in the repository

Publisher copyright

(Article begins on next page)

06 October 2026

Atmospheric Environment 367 (2026) 121748

Contents lists available at ScienceDirect

Atmospheric Environment

journal homepage: www.elsevier.com/locate/atmosenv

Three-dimensional pollutant dispersion in tree-lined urban canyons: Combined wind-tunnel and LES analysis

Sofia Fellini [a,*], Dipanjan Majumdar [b], Pietro Salizzoni [c,a], Maarten van Reeuwijk [b]

[a] Department of Environmental, Land and Infrastructure Engineering (DIATI), Politecnico di Torino, Corso Duca degli Abruzzi 24, 10129 Turin, Italy
[b] Department of Civil and Environmental Engineering, Imperial College London, London, SW7 2AZ, UK
[c] Ecole Centrale de Lyon, CNRS, Universite Claude Bernard Lyon 1, INSA Lyon, LMFA, UMR5509, 69130, Ecully, France

HIGHLIGHTS

- LES and wind-tunnel data reveal 3D pollutant dispersion in street canyons.
- Vegetation modifies turbulence, increasing spanwise pollutant variability.
- Average street pollution shows no systematic dependence on tree number or drag.
- Tree drag tuning aligns numerical simulations with experimental measurements.
- Integrated experimental–numerical approach advances urban air quality modeling.

GRAPHICAL ABSTRACT

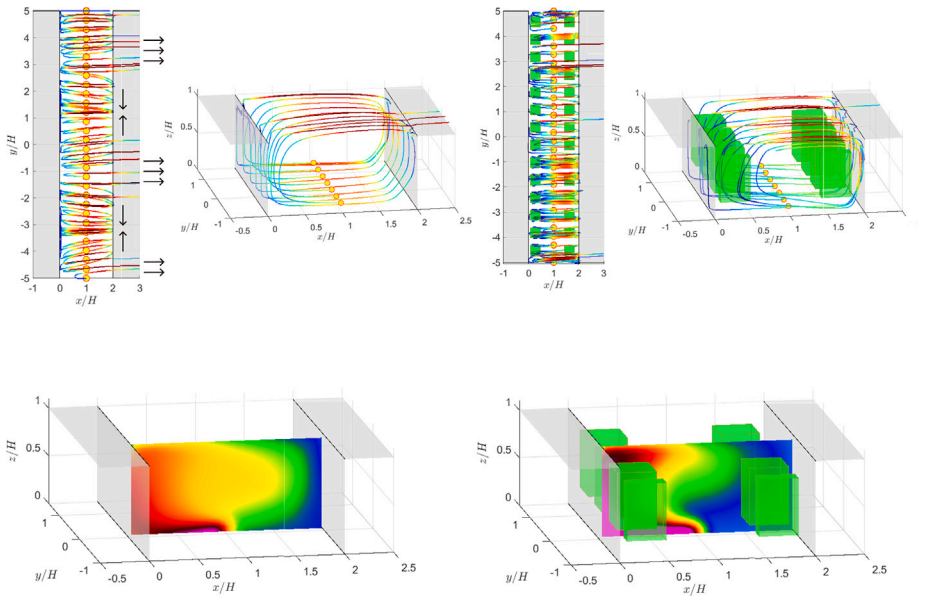

ARTICLE INFO

Dataset link: https://zenodo.org/records/15633150

Keywords:
Vegetated street canyon
Street canyon ventilation
Urban air pollution
Pollutant dispersion

ABSTRACT

Vegetation is increasingly used in urban areas to improve microclimate and reduce pollutant exposure, yet its effect on pollutant dispersion within street canyons remains complex. This study combines high-resolution wind tunnel experiments and Large-Eddy Simulations (LES) using uDALES to provide a detailed three-dimensional characterization of airflow and pollutant concentration along the canyon.

Special attention is given to the consistent scaling of velocity and scalar fields, using friction velocity and canyon geometry as reference quantities, and to the role of tree drag length in aligning the aerodynamic resistance of physical and numerical vegetation. The simulations reproduce key mean-flow structures, including large-scale recirculations, but tend to underestimate turbulent kinetic energy and local scalar fluxes.

By jointly analyzing high-resolution wind-tunnel experiments and LES, we (i) confirm the spanwise and longitudinal concentration patterns observed experimentally, (ii) assess their sensitivity to the modeled tree

* Corresponding author.
E-mail address: sofia.fellini@polito.it (S. Fellini).

https://doi.org/10.1016/j.atmosenv.2025.121748
Received 13 September 2025; Received in revised form 3 December 2025; Accepted 14 December 2025
Available online 16 December 2025
1352-2310/© 2025 The Authors. Published by Elsevier Ltd. This is an open access article under the CC BY license (http://creativecommons.org/licenses/by/4.0/).

drag, (iii) provide the first detailed experimental–numerical comparison of rooftop mean and turbulent mass fluxes, showing that bulk canyon ventilation exhibits no systematic dependence on tree number or drag intensity, and (iv) identify the specific strengths and limitations of each approach. This integrated analysis offers novel insights into the interplay between trees, turbulence, and boundary-layer forcing, informing strategies for modeling urban ventilation and pollutant dispersion in tree-lined streets.

1. Introduction

Urban air pollution and heat stress are among the most pressing challenges in modern cities. In densely built environments, street canyons—urban corridors flanked by continuous buildings—tend to trap traffic-emitted pollutants, where restricted ventilation hinders their removal (Vardoulakis et al., 2003; Salizzoni et al., 2009; Fellini et al., 2020). Urban vegetation is increasingly promoted as a nature-based strategy to mitigate these adverse effects. Trees in particular can improve thermal comfort through shading and evapotranspiration and remove airborne pollutants via dry deposition (Janhäll, 2015; Santiago et al., 2017; Revelli and Porporato, 2018; Busca and Revelli, 2022). However, trees also modify flow dynamics, acting as porous obstacles that increase drag and potentially hinder ventilation and pollutant dispersion within street canyons (Abhijith et al., 2017; Grylls and van Reeuwijk, 2022). Depending on vegetation density, crown porosity, and arrangement, the net effect of trees can be either beneficial or detrimental to local air quality (Jeanjean et al., 2017; Grylls and van Reeuwijk, 2022; Maison et al., 2024).

Beyond the average pollution level in the street, urban air quality is critically shaped by the spatial distribution of pollutants within the canyon, which determines where high-exposure zones arise. This distribution is controlled by how turbulence and secondary flows transport pollutants across the canyon volume, and is strongly modulated by the presence of trees. Recent high-resolution wind-tunnel measurements have revealed spanwise heterogeneity in tree-lined canyons (Fellini et al., 2022; Del Ponte et al., 2024; Fellini et al., 2025), with alternating accumulation zones and low-concentration corridors repeating along the canyon axis. Such patterns have been consistently observed across different geometrical configurations, including a continuous canyon extending along the wind-tunnel length, a short canyon with lateral intersections, and a long canyon laterally closed. In addition to vegetation, spatial variability can also arise from spanwise modulations of the overlying boundary layer, particularly above cubic-like roughness elements such as buildings (Reynolds et al., 2007; Perret and Savory, 2013; Vanderwel and Ganapathisubramani, 2015; Perret et al., 2019). These secondary motions may penetrate into the urban canopy and couple with canyon recirculation. Understanding whether such patterns arise within street canyons, how they interact with vegetation, and whether they control ventilation pathways is fundamental for assessing pollutant exposure and evaluating the effectiveness of urban greening strategies.

Even with advanced instrumentation, wind-tunnel experiments provide only a partial picture. The limited number of measurement points and the physical constraints of instrumentation hinder a full three-dimensional characterization of flow and scalar fields. Near-wall regions, which are especially critical for pedestrian exposure, are particularly challenging: steep concentration gradients and restricted experimental access make them difficult to resolve reliably.

Numerical simulations, particularly Reynolds-Averaged Navier–Stokes (RANS) and Large-Eddy Simulations (LES), can complement experiments by providing continuous, three-dimensional fields of velocity and concentration. RANS models have been extensively applied to urban canopies to estimate mean flow and pollutant distributions in both idealized and realistic configurations (e.g., Gromke et al., 2008; Buccolieri et al., 2011; Jeanjean et al., 2015). However, their reliance on simplified turbulence closures and schematic representations of vegetation limits their ability to capture unsteady mixing processes. By resolving large turbulent structures, LES offers a more faithful description of the interaction between vegetation drag, coherent eddies, and scalar transport (Salim et al., 2011; Moonen et al., 2013; Merlier et al., 2018). Still, LES outcomes remain highly sensitive to how vegetation is parameterized (e.g., drag coefficient, morphology, spatial distribution) (Buccolieri et al., 2018; Fu et al., 2024; Majumdar et al., 2025). Another critical aspect is the consistency between experimental and numerical boundary layers: reproducing friction velocity, turbulence intensity, and boundary-layer depth is essential to ensure dynamically meaningful comparisons. In this respect, scaling flow and scalar fields with appropriate reference quantities, and ensuring consistency in the aerodynamic resistance of trees across physical and numerical representations, are key to establishing a robust comparison framework (Gromke, 2011).

For these reasons, experiments and simulations should be viewed as complementary rather than alternative approaches. On one side, simulations can be validated and constrained by experimental evidence; on the other, experiments gain interpretative power through the three-dimensional, highly resolved insights offered by LES. This reciprocity is particularly valuable when assessing urban ventilation, where both mean transport and turbulent exchange contribute to pollutant removal, especially in the presence of vegetation, whose aerodynamic effects require explicit and carefully parameterized representation in simulations.

Previous comparisons between numerical models and wind-tunnel data have mainly focused on basic diagnostics. RANS validations have typically been restricted to mean wall concentrations and velocity fields in single cross-sections of street canyons, with or without trees (Gromke et al., 2008; Buccolieri et al., 2011; Jeanjean et al., 2015). LES validations have likewise often focused on wall concentrations or on a limited set of vertical profiles, both for empty canyons (Llaguno-Munitxa et al., 2017; Chatzimichailidis et al., 2019; Zheng et al., 2021) and for vegetated canyons, where tree porosity effects were also explored (Salim et al., 2011; Moonen et al., 2013; Merlier et al., 2018). More advanced LES assessments have been attempted in canyons without trees, for example through comparisons with time-resolved PIV in wind-tunnel experiments (Kellnerová et al., 2018), or in the field for vegetated street canyons (Resler et al., 2021). Overall, the majority of the validations discussed above have primarily retained a quasi-2D perspective and examined an isolated canyon within a rough-wall boundary layer, rather than a canyon embedded in a continuous urban canopy. Consequently, they could not capture the spanwise flow structures that develop above building canopies and may modulate in-canyon pollutant dispersion. Despite recent progress, it remains unclear whether LES can capture the spanwise heterogeneity and longitudinal organization of pollutant fields revealed by high-resolution wind-tunnel studies of tree-lined canyons (Fellini et al., 2022; Del Ponte et al., 2024).

The present work addresses this gap by combining high-resolution wind-tunnel experiments with LES within a consistent framework. The comparison extends beyond conventional diagnostics based on single profiles or wall measurements, encompassing three-dimensional velocity and concentration fields both within and above the canyon. Specifically, our objectives are to: (i) evaluate whether LES can reproduce the spanwise and longitudinal concentration patterns identified experimentally; (ii) investigate the sensitivity of these patterns to the parameterization of tree drag; (iii) conduct, for the first time, a detailed experimental–simulation comparison of rooftop mean and turbulent mass fluxes across the canyon–atmosphere interface, in order to assess whether LES captures the ventilation processes that govern pollutant

exchange; and (iv) determine whether experiments and simulations provide consistent insights into the role of vegetation in modulating overall canyon ventilation, thereby delineating the specific strengths and limitations of each approach.

By pursuing these objectives, we aim to clarify how the interplay between trees, turbulent structures, and boundary-layer forcing influences canyon ventilation, and to establish a cross-methodological framework for urban air quality modeling.

2. Methodology

2.1. Wind tunnel experiment

The experiments (Fellini et al., 2022; Del Ponte et al., 2024) were conducted in the atmospheric wind tunnel at the Laboratoire de Mécanique des Fluides et d'Acoustique (LMFA) at the École Centrale de Lyon. The wind tunnel's test section (Fig. 1) was 12 m in length, 3.5 m in width, and 2 m in height. To reproduce an urban-like rough boundary layer, the floor was covered with an array of wooden and polystyrene blocks (50 cm wide, 10 cm high), spaced 10 cm apart in the spanwise direction and 20 cm in the streamwise direction. This generated a regular network of square street canyons with $H/W = 1$ (where H is the building height and W the street width), intersected by wider perpendicular canyons ($H/W = 0.5$). This configuration was chosen to avoid channeling effects and to replicate tree-lined boulevards (Fellini et al., 2022). The incoming boundary layer was allowed to develop along 9 m of roughness fetch before reaching the reference canyon, ensuring a fully rough turbulent regime.

The reference canyon, perpendicular to the wind direction, was located at a distance of approximately 9 m from the beginning of the test section and had dimensions $L = 1.0$ m (canyon length), $W = 0.2$ m, $H = 0.1$ m (Fig. 1.b). Lateral closures with polystyrene blocks confined the canyon spanwise extent, enabling the definition of a control volume for rooftop mass balance calculations (see Section 4.6). The previous work by Fellini et al. (2022) has shown that spanwise closures do not significantly alter the transverse structure of the flow or dispersion patterns when compared to an effectively infinitely long canyon, ensuring that the observed flow features are representative of a fully developed canyon.

We adopt a Cartesian coordinate system (x, y, z), where x is the streamwise direction(aligned with the incoming wind (with $x = 0$ at the upwind wall of the reference canyon), y is the spanwise direction (perpendicular to the wind, with $y = 0$ at the canyon centerline), and z is the vertical direction (with $z = 0$ at the street floor).

Urban vegetation was represented by porous plastic model trees arranged in two lateral rows. Each tree had a crown of width and depth $W_C = L_C = 4.5$ cm and height $H_C = 6.5$ cm, mounted on a 2 cm trunk for a total height $H_T = 8.5$ cm (Fig. 1.c). Three tree densities were tested: *zero* (no trees), *half* (7 trees per row, trunk spacing 14 cm), and *full* (14 trees per row, spacing 7 cm). Aerodynamic properties of the trees were independently characterized in a small-scale wind tunnel (see Section 3.2).

Pollutant emissions were simulated by a linear ethane source, 65 cm long (L_s), positioned at street level along the canyon axis (yellow line in Fig. 1). The source design ensured uniform lateral release (Marro et al., 2020).

Concentrations were measured using a Flame Ionization Detector (FID) with a constant sampling frequency of 1000 Hz. For each sampling point, we fixed an acquisition time of 2 min which was assessed to provide a reliable estimate of the mean concentration. Moreover, before and after each acquisition, the background concentration was recorded by stopping the emission for 15 s (and leaving time for the transients to settle). The velocity field was characterized above the obstacles by two-component Hot-Wire Anemometry (HWA) at 4000 Hz with a 1-minute acquisition time, and within the canyon by a three-component Laser Doppler Anemometer (LDA). The LDA was coupled with the FID to resolve vertical turbulent mass fluxes inside the canyon and at the roof. Typical acquisition rates were 1500 Hz, with at least 250,000 samples per point. LDA–FID synchronization and cross-correlation procedures followed the methodology of Marro et al. (2020). For each sampling point, the full measurement window was used to compute flow statistics, and convergence up to second-order moments was verified (see Fellini et al. (2022) and Del Ponte et al. (2024) for more details).

2.2. uDALES simulations

Numerical simulations were performed with uDALES, a multi-physics micro-climate modeling framework specifically developed for studying the built environment at microscale resolution (Suter et al., 2022; Owens et al., 2024). uDALES has been successfully validated against controlled laboratory experiments, including studies of pollutant dispersion around tall-building clusters (Lim et al., 2022).

The code performs LES of the incompressible Navier–Stokes equation under the Boussinesq approximation. The turbulence is resolved up to the grid scale and the subgrid-scale (SGS) turbulence is modeled following Vreman (2004). The SGS eddy diffusivity for the passive scalar is computed from the SGS eddy viscosity through a constant turbulent Prandtl number, $Pr_t = 0.33$, consistent with recommendations for neutral-flow LES (Deardorff, 1980; Dai et al., 2021). The effects of urban surfaces are modeled in terms of a novel conservative immersed boundary method (Owens et al., 2024). The building geometry is specified as a triangulated surface which consists of a list of triangular facets in terms of their three vertices in 3D Cartesian space. Wall functions are used to model surface fluxes (e.g., shear stress) which are then converted to appropriate source/sink terms to apply in the right hand side of the momentum equation (Owens et al., 2024).

uDALES is equipped with a 'grey-scale' tree model, capable of simulating tree drag, deposition, shading and evaporation (Grylls and van Reeuwijk, 2021). Trees are represented in the domain by volumetric cuboid blocks consisting of several computational grid cells. The combined inertial and viscous losses due to the tree presence are modeled through a volumetric momentum sink term applied directly into the right-hand side of the governing equation at those grid cells which fall within the tree block. The momentum sink $\mathbf{S_u}$ can be expressed as (Finnigan, 2000):

$$\mathbf{S_u} = -aC_d^V|\mathbf{u}|\mathbf{u}\,, \tag{1}$$

where C_d^V is the volumetric drag coefficient, $\mathbf{u}$ is the local velocity, and a is the one-sided leaf-area density. Here, the "one-sided" leaf-area density refers to the leaf area per unit canopy volume computed by considering only one side of each leaf (i.e., half of the total physical leaf area). This definition follows standard practice in canopy-flow modeling (Oke et al., 2017). Representative values for the parameters a and C_d^V account for the natural variability due to different tree species, sizes, ages and meteorological conditions (see Section 3.2 for the adopted values in this study).

uDALES simulation follows the experimental set-up and tree arrangements exactly except the fact that the computational set-up dimensions in uDALES is full-scale (m scale), i.e. the dimensions are 100 times larger than the experimental scale (cm scale); see Fig. 1. The computational domain size is $L_x \times L_y \times L_z = 1200$ m $\times$ 360 m $\times$ 110 m, and the number of grid points is $N_x \times N_y \times N_z = 2400 \times 720 \times 220$, resulting in a uniform 0.5 m resolution in all directions. Thus, along the z-direction, 20 grid points are resolved within the street canyon and 13 within the tree crown. The adopted resolution of 0.5 m is consistent with recommendations for obstacle-resolving LES (e.g., Xie and Castro, 2006) and comparable to recent uDALES studies of vegetated canyons (e.g., Grylls and van Reeuwijk, 2022). Importantly, this resolution was selected to provide sufficient detail at the street scale while accurately reproducing the boundary layer above the entire three-dimensional urban canopy, making it possible

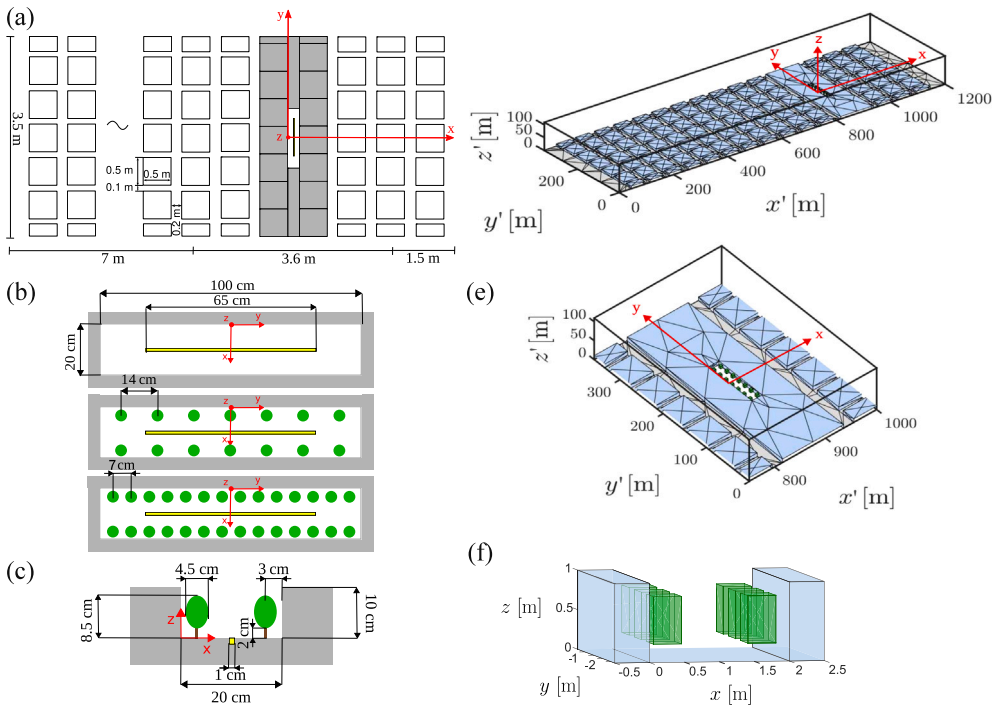

Fig. 1. (a) Sketch of the urban canopy in the test section of the tunnel. The blocks delimiting the reference street canyon are colored gray. (b) Top view of the street canyon model for different tree density configurations: *Zero*, *Half*, *Full*, where the yellow line represents the pollutant source. (c) Sketch of the front view of the street. (d) Computational domain in uDALES. (e) Top and (f) front views of the street canyon (*Half* configuration) in the computational domain. The coordinate system is shown in red.

to investigate potential secondary flows within the boundary layer. The good agreement with wind-tunnel data (see Section 4) further supports the suitability of this choice.

In order to solve the flow governing equations, periodic lateral boundary conditions are applied in both x and y directions, whereas a free-slip condition is used at the top of the computational domain. A no-slip condition is imposed at all building and street surfaces via wall functions. The use of periodic lateral boundaries for the velocity field in neutral ABL LES is standard and widely accepted in the literature (Stoll et al., 2020; Nazarian et al., 2020; Auvinen et al., 2020; Blunn et al., 2022). Even though periodic boundaries prevent perturbations from exiting the domain, a statistically steady state is achieved as shear production is balanced by surface drag and SGS dissipation after the initial transient.

For the pollutant concentration, an inflow–outflow boundary condition is applied instead along the x-direction to prevent scalar accumulation within the domain. This consists of a Dirichlet condition ($c = 0$) at the inlet and a convective outflow condition ($\partial c/\partial t + u_{\text{out}}\,\partial c/\partial x = 0$) at the outlet, where u_{out} is the area-averaged outflow velocity along x. The scalar concentration evolves passively and does not influence the flow-field solution.

In the uDALES simulations, the wind is driven by a constant pressure gradient along x-direction,

$$\frac{\partial P}{\partial x} = -\frac{\rho u_*^2}{L_z}\,, \tag{2}$$

where $\rho = 1.2$ kg/m^3 is the air density and $u_* = 0.253$ m/s is the domain-averaged friction velocity. Formally, the denominator should be expressed as $V_f/(L_x L_y)$, where V_f is the volume occupied by the fluid within the domain. However, for sufficiently small blockage ratios, this approximation introduces negligible error and the use of L_z remains valid. The pressure gradient is added as a body force to the streamwise momentum equation.

The flow simulation is advanced in time using an adaptive time-stepping, limited by both the Courant–Friedrichs–Lewy criterion and the diffusion number. The total simulation time corresponds to 346 characteristic time scales, defined as $T = H/u_*$, which represents the typical time for momentum to be transferred across the canyon height. Statistical averages were computed over the last half of the simulation ($\approx 173T$). This averaging period is longer than those commonly used in similar studies (e.g., Xie and Castro, 2006) and was verified to yield stable mean and turbulent statistics throughout the canyon and the roughness sub-layer.

For the pollutant emission, uDALES uses a volumetric scalar source model. A line source is assumed to be at the same location on the ground within the canyon and of the same length as was in the experimental setup. We assume that the influence of this line source is seen by the surrounding grid points, following a Gaussian distribution around the line source, i.e. the scalar input is maximum on the given line source and its influence decreases exponentially as the distance between the grid points and the line source increases. In our numerical implementation the influence of the line source is seen only at the grid points that are within 3σ [m] distance from the line source; σ [m] being the standard deviation. Thus, any grid point at a perpendicular distance of r [m] from the line source gets influenced by the line source segment between $-\sqrt{9\sigma^2 - r^2}$ and $\sqrt{9\sigma^2 - r^2}$. Denoting the strength of the line source as S $\left[\text{g m}^{-1}\ \text{s}^{-1}\right]$, the rate of concentration c_{cell} $\left[\text{g m}^{-3}\ \text{s}^{-1}\right]$ exerted at any grid point is given by,

$$\begin{aligned} c_{\text{cell}} &= \int_{-\sqrt{9\sigma^2-r^2}}^{\sqrt{9\sigma^2-r^2}} \frac{S}{\Delta x\,\Delta y\,\Delta z}\, e^{-(r^2+l^2)/2\sigma^2}\,\mathrm{d}l \\ &= (2\pi)^{1/2}\,\frac{S}{\Delta x\,\Delta y\,\Delta z}\,\sigma\, e^{-r^2/2\sigma^2}\,\mathrm{erf}\left(\sqrt{\frac{9\sigma^2 - r^2}{2\sigma^2}}\right)\,, \end{aligned} \tag{3}$$

where $\Delta x \times \Delta y \times \Delta z$ $\left[\text{m}^3\right]$ is the volume of the grid cell, and $\mathrm{erf}(\cdot)$ indicates the Gaussian error function. The rate of total amount of scalar going into the computational domain Q_{et}^{uDALES}[g/s] is given by,

$$Q_{et}^{\text{uDALES}} = \int_0^{\infty}\int_0^{\frac{\pi}{2}}\int_0^{2\pi}\int_0^{L_s} \frac{S}{\Delta x\,\Delta y\,\Delta z}\, e^{-r^2/2\sigma^2}\, r^2 \sin\phi\,\mathrm{d}l\,\mathrm{d}\theta\,\mathrm{d}\phi\,\mathrm{d}r$$

$$= \frac{2^{1/2}\pi^{3/2} S L_s \sigma^3}{\Delta x\, \Delta y\, \Delta z}. \quad (4)$$

3. Aligning wind tunnel experiments with LES

3.1. Urban boundary layer

The interaction between the canyon and the overlying turbulent boundary layer plays a central role in determining flow and pollutant exchange processes in the streets. Ensuring comparability between wind tunnel (WT) and LES therefore requires particular care in reproducing the boundary layer.

In the WT, the boundary layer developed over an idealized urban canopy composed of regularly spaced blocks, with Irwin spires at the inlet and metallic nuts on the rooftops enhancing surface roughness (Irwin, 1981; Fellini et al., 2022). Measurements showed that the flow approached quasi-equilibrium near the reference canyon, with a boundary-layer thickness of $\delta \approx 1.1$ m ($\delta/H \approx 11$), consistent with atmospheric conditions (Perret et al., 2019). The free-stream velocity was $U_\infty = 5$ m/s, yielding $Re_H = 1.25 \times 10^4$. Above the roughness sublayer, a logarithmic inertial layer was observed; fitting this region gave a friction velocity $u_* = 0.29$ m/s, with displacement height $d = 0.094$ m and roughness length $z_0 = 10^{-3}$ m. See Fellini et al. (2022) for more details.

In uDALES, the flow is generated using a prescribed pressure gradient that drives the flow along the x-direction, as described in Section 2.2. The periodic boundary conditions in both horizontal directions, the free-slip condition at the top of the domain, and the no-slip boundary condition at all solid surfaces lead to the formation of a fully developed boundary layer. In this setup, the domain average streamwise velocity, $\langle u \rangle_{xy} = (L_x L_y)^{-1} \int_0^{L_y} \int_0^{L_x} \overline{u}\, \mathrm{d}x\, \mathrm{d}y$, reaches a value of $\langle u \rangle_{xy}|_{z=L_z} = 4.36$ m/s at the top of the domain, and $\langle u \rangle_{xy}|_{z=H} = U_H = 0.692$ m/s at the building height. To ensure consistency with the WT, the local u_* was obtained from the Reynolds shear stress profile in the inertial sublayer, giving $u_* = 0.24$ m/s.

These differences in boundary-layer formation underline that WT and LES inevitably differ in scale and turbulence-generation mechanisms: the WT produces a developing boundary layer, whereas LES yields a fully developed one. Consequently, scaling with U_∞, as commonly done in experimental and numerical studies (e.g., Allegrini et al., 2013; Peng et al., 2020; Fellini et al., 2022), is not appropriate here, since U_∞ does not exist in a fully developed boundary layer. More importantly, accurately scaling turbulence is essential for capturing flow dynamics within the canyon. In shear layers (and in the absence of buoyancy), turbulence is typically proportional to the friction velocity u_* (Pope, 2000), which therefore serves as the appropriate reference velocity for our comparison. However, for this scaling to be valid, the canyon flow in both the experiment and simulation must be in a Reynolds number–independent regime. This condition is met when $Re_H = U_H H/\nu > 10^3$ (Shu et al., 2020), where U_H is the characteristic velocity at roof height (H), and ν the kinematic viscosity of air. This condition is satisfied in the here presented wind tunnel experiments. The LES is independent of Reynolds number by definition as neither the turbulence model nor the wall-functions rely on the molecular viscosity of the fluid.

Fig. 2 compares vertical profiles of mean and turbulent quantities in the inertial sublayer from uDALES (lines) and WT data (symbols). Experimental profiles were sampled at four horizontal locations within a geometrically periodic unit, defined as the smallest repeating element of the building array (gray area in the inset in Fig. 2.a). This unit consists of one square building together with the characteristic street widths that separate it from its neighbors: $H/W = 1$ in the streamwise (parallel-to-wind) direction and $H/W = 0.5$ in the spanwise (perpendicular-to-wind) direction. Sampling within this unit captures the flow variability associated with the two canyon orientations. LES results were averaged over the corresponding area of the computational domain.

The mean velocity profile (Fig. 2.a), normalized by u_*, shows a logarithmic region above the canopy ($z/H > 2$) in both datasets, indicating a well-developed inertial layer. The Reynolds shear stress $\overline{u'w'}/u_*^2$ (Fig. 2.b) forms the expected plateau in LES, while WT values show greater scatter, partly due to the known 10%–20% underestimation of hot-wire anemometry (HWA). For this reason, u_* from WT data was not derived from the Reynolds stress, but instead obtained by fitting the mean velocity profile to the logarithmic law, as described earlier.

Standard deviations of velocity components (Fig. 2.c) reveal that LES slightly overestimates σ_u and underestimates σ_v and σ_w, yet captures the overall turbulence trends. The resulting turbulent kinetic energy, defined as $k = (\sigma_u^2 + \sigma_v^2 + \sigma_w^2)/2$, profiles (Fig. 2.d) are in reasonable agreement, though LES slightly underestimates k near the rooftop ($z/H \approx 1$), implying reduced turbulence levels within the canyon compared to WT.

Slight discrepancies in the velocity standard deviations and in k near the rooftop height ($z/H \approx 1$) can be explained by several factors. First, underestimation of k and fluctuation intensities in the near-wall region is a well-known limitation of LES, consistently reported in previous studies (Nakajima et al., 2018; Ikegaya et al., 2019; Wang et al., 2021), and generally attributed to grid resolution constraints, the absence of turbulent inflow, and the difficulty of resolving wall-generated turbulence in complex geometries (see also Section 4.3). Second, in the wind tunnel, additional roughness was introduced by metallic nuts placed on building rooftops to promote boundary-layer development (Salizzoni et al., 2008). This treatment likely enhanced turbulence locally around $z/H \approx 1$, contributing to the higher k observed experimentally. Third, differences in boundary-layer development may also play a role: while the WT layer was slowly evolving in the streamwise direction, the use of periodic boundaries in uDALES enforced a statistically stationary state and provided greater averaging convergence. These contrasting conditions further explain the discrepancies between the two datasets.

Accurate representation of turbulence is crucial for correctly capturing pollutant dispersion processes (Jiao and Takemi, 2024, 2025). Later in Section 4, we will discuss how the observed underestimation of turbulent kinetic energy affects the k inside the canyon, the canyon-scale concentration fields, and the overall ventilation efficiency.

3.2. Tree drag

The reduced-scale model trees used in the wind tunnel experiments were characterized by estimating their drag coefficient (C_d) and aerodynamic porosity (α_L), following the approach of Manickathan et al. (2018). The classical drag coefficient was defined as

$$C_d = \frac{2F_d}{\rho_a U_{\mathrm{ref}}^2 A_f}, \quad (5)$$

where F_d is the bulk drag force measured on a single tree, ρ_a the air density, U_{ref} the upstream reference velocity, and A_f the projected frontal area. The force was measured in a closed-circuit wind tunnel with a 30×30 cm test section using a load cell, while U_{ref} was obtained from a Pitot tube (Fellini et al., 2022). The frontal area was extracted from tree images processed into binary masks and refined using the alpha-shape method (Zhu et al., 2021). This yielded $A_f = 0.0021$ m^2.

In Fig. 3.b the experimental drag coefficient is shown as a function of the tree Reynolds number ($Re_T = U_{\mathrm{ref}} H_T/\nu$, where H_T is the tree height), for four different faces of a single model tree, obtained by rotating the tree's vertical axis in 90° intervals. Except for the values at low speeds (where the experimental uncertainty is large), the drag coefficient rapidly converges to 1.07.

The aerodynamic porosity α_L (Guan et al., 2003) was estimated as

$$\alpha_L = \frac{\iint_{A_f} \overline{u}(L_C, y, z)\, \mathrm{d}y\, \mathrm{d}z}{\iint_{A_f} U_{\mathrm{ref}}\, \mathrm{d}y\, \mathrm{d}z}, \quad (6)$$

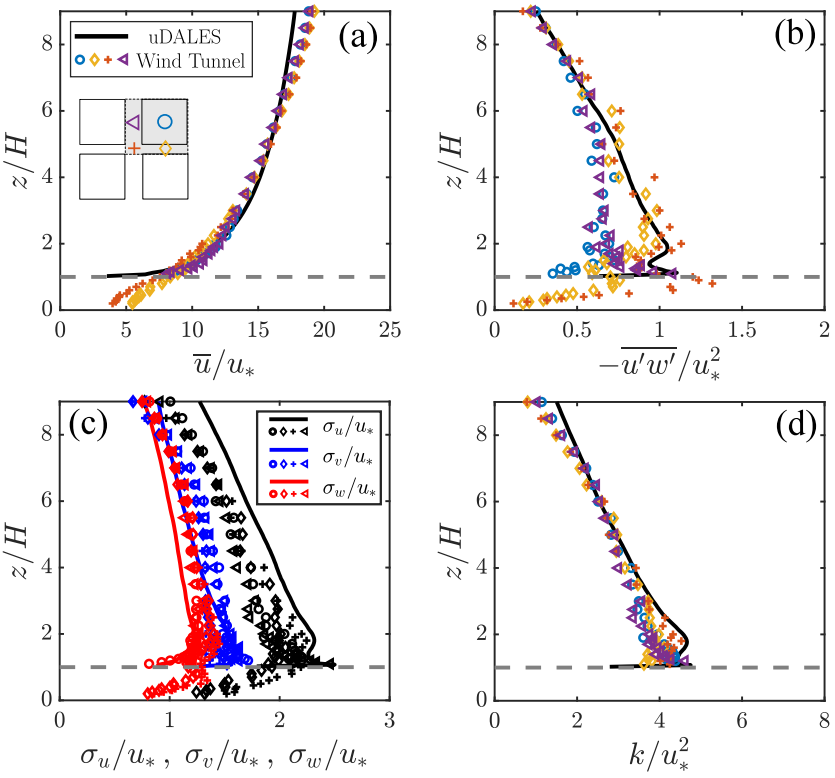

Fig. 2. Vertical profiles of turbulent quantities: (a) mean streamwise velocity $\overline{u}/u_*$, (b) Reynolds shear stress $-\overline{u'w'}/u_*^2$, (c) turbulent kinetic energy k/u_*^2, and (d) standard deviations of velocity components σ_u/u_* (black), σ_v/u_* (blue), σ_w/u_* (red). Markers represent wind tunnel measurements at four (x, y) positions within a spatially periodic unit (see the gray area in the inset in panel a). Black lines denote uDALES profiles averaged over the same horizontal locations. The horizontal dashed line indicates the canyon height H.

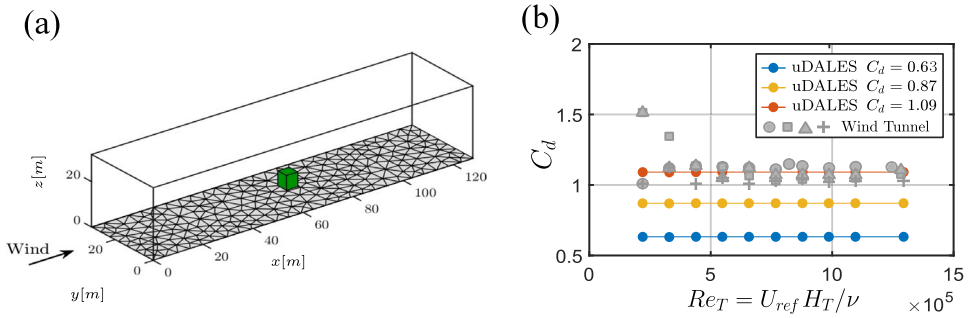

Fig. 3. (a) Numerical setup for estimating the bulk drag coefficient. (b) Drag coefficient as a function of Re_T for different leaf area density (and drag lengths). The experimental C_d was measured for four different alignments (reported by different markers) of a single model tree, obtained by rotating the vertical axis of the tree at 90° intervals. Numerical simulations were performed keeping $C_d^V = 0.2$ as a constant.

where $\overline{u}(L_C, y, z)$ is the time-averaged velocity measured downstream of the tree ($x = L_C$). This parameter quantifies the fraction of airflow passing through the tree crown relative to the airflow diverted around it. Velocity measurements were performed on a dense grid behind the tree, and spatial interpolation was used to properly estimate $\overline{u}(L_C, y, z)$. The aerodynamic porosity for a single tree was found to be approximately 0.26.

As mentioned in Section 2.2, the drag exerted by trees is modeled in uDALES as a volumetric sink term parameterized using a and C_d^V (Eq. (1)). Note that the volumetric drag coefficient C_d^V used in the numerical simulation is different from the classical drag coefficient C_d measured from wind tunnel experiment using Eq. (5), and it is not straightforward to map one onto the other. Majumdar et al. (2025) recently developed an analytical model linking the parameters typically used in wind tunnel experiments (C_d, α_L) with those adopted in CFD simulations (a, C_d^V). They identified the drag length, $\ell_d = (aC_d^V)^{-1}$, as the key metric to characterize local tree drag, and derived the following relation between ℓ_d and aerodynamic porosity:

$$\ell_d \left[1.27 + 0.55 \left(\frac{W_C H_C}{\ell_d^2} \right)^{0.33} \right] = -\frac{2L_C}{\ln(\alpha_L^2)} \tag{7}$$

where, as a reminder, W_C and H_C are the width and height of the tree crown. Applying this formulation to the model trees used here ($L_C = W_C = 4.5$ cm, $H_C = 6.5$ cm, $\alpha_L = 0.26$) gives $\ell_d = 1.2$ cm. For the full-scale uDALES simulations, the ℓ_d must be scaled according to geometric scaling (Majumdar et al., 2025), hence for the simulations $\ell_d = 1.2$ m. With $C_d^V = 0.2$ (Buccolieri et al., 2018), this implies a leaf area density $a = (\ell_d C_d^V)^{-1} = 4.14$ m^2/m^3. As pointed out in Majumdar et al. (2025), the full-scale ℓ_d of the model trees used in experiments is

significantly lower than values reported in field studies (they estimate $10 < \ell_d < 34$ m), which may lead to an overestimation of the drag effect imposed by trees.

To validate the proposed approach for matching tree drag in uDALES, we performed a dedicated simulation replicating the small wind tunnel setup where a single model tree was characterized (Fig. 3.a). According to the methodology described above, the tree was represented as a cuboid with properties $C_d^V = 0.2$ and $a = 4.136$ m^2/m^3. The total drag force F_d exerted on the tree was obtained by integrating the momentum sink term S_u (Eq. (1)) over the tree volume:

$$F_d = \rho_a \int_V S_u \, \mathrm{d}V, \tag{8}$$

and converted into a bulk drag coefficient,

$$C_d = \frac{2F_d}{\rho_a U_{\mathrm{ref}}^2 A_{\mathrm{f}}} = \frac{2\int_V S_u \, \mathrm{d}V}{U_{\mathrm{ref}}^2 A_{\mathrm{f}}}. \tag{9}$$

The simulation yielded $C_d = 1.09$, in excellent agreement with the experimental value of 1.07 (Fig. 3b). The aerodynamic porosity computed from the simulated velocity field ($\alpha_L = 0.28$) also closely matched the measured value (0.26). As expected, no Reynolds-number dependence was observed in uDALES, since the canopy model does not rely on molecular viscosity. These results confirm that the drag length is the key parameter for reproducing tree drag in LES.

For the uDALES simulations, the experimentally derived $\ell_d = 1.2$ m was taken as the reference case. To explore sensitivity and to represent more realistic vegetation properties, two additional values were considered: $\ell_d = 4.9$ m and $\ell_d = 10.2$ m. These values, are more consistent with the range reported in field studies (10–30 m, Majumdar et al. (2025)), and correspond to weaker aerodynamic resistance. As discussed later, these reduced-drag cases improved the match with wind-tunnel concentration patterns, highlighting the strong sensitivity of canyon ventilation to vegetation drag.

4. Wind-tunnel – LES comparison

This section presents a systematic comparison between wind tunnel experiments and uDALES simulations for different canyon configurations, with and without vegetation. The goals are (i) to evaluate the ability of uDALES to reproduce experimentally observed flow and dispersion patterns, and (ii) to investigate how vegetation drag influences mean flow structures, turbulence, scalar concentrations, and ventilation efficiency.

Table 1 summarizes the analyzed cases. Three experimental setups with increasing tree density were reproduced in LES, each identified by a label (*Id*) encoding the setup type (E for experiment, S for simulation), the vegetation density — *z* (zero), *h* (half), or *f* (full) — and the drag length ℓ_d, rounded to the nearest meter (1, 5, or 10). For clarity, the discussion mainly focuses on the *zero* and *full* cases, which represent the two extreme vegetation scenarios. The mean fields analyzed in the following sections represent time-averaged values, obtained at each grid point (numerical) or measurement location (experimental), using the averaging periods described in Sections 2.1 and 2.2.

4.1. Vertical profiles of mean flow and turbulent kinetic energy inside the canyon

Fig. 4 presents vertical profiles of key flow quantities simulated in uDALES, spanwise-averaged (y) and extracted at the canyon centerline ($x/H = 1$). Results are shown for the empty canyon (S*z*, in orange) and for the densely vegetated cases (S*f*1, S*f*5, S*f*10, in blue). The LES results are compared with wind tunnel measurements for the corresponding configurations (E*z*, E*f*).

Panel (a) shows the mean streamwise velocity ($\overline{u}$), which displays the characteristic S-shape, with positive peaks near rooftop height and negative values in the lower canyon. Vegetation mainly affects the lower part of the canyon, where tree drag slows down the recirculating flow.

Table 1
Summary of experimental and numerical configurations for the three canyon setups: an empty canyon (*zero-z*), a sparsely vegetated canyon (*half-h*), and a densely vegetated canyon (*full-f*). The *Id* encodes the Experiment or Simulation type (E/S), the canyon configuration (*z*/*h*/*f*), and an integer indicating the drag length in meters. In the experiment, each plastic tree has dimensions $H_T = 8.5$ cm, $W_C = L_C = 4.5$ cm, and $H_C = 6.5$ cm. In the simulations, each tree is modeled as a cuboid with $W_C = L_C = 4.5$ m and $H_C = 6.5$ m, with the base starting 2 m above ground level.

Setup	Id	Type	N° trees	ℓ_d [m]	C_d^v	a [m^2/m^3]	C_d	α_L
Empty *zero* (*z*)	E*z*	Exp	0	–	–	–	–	–
	S*z*	Sim	0	–	–	–	–	–
Sparsely vegetated *half* (*h*)	E*h*	Exp	14	1.2×10^{-2}	–	–	1.07	0.26
	S*h*1	Sim	14	1.2	0.2	4.14	1.09	0.28
	S*h*5	Sim	14	4.9	0.2	1.02	0.87	0.53
	S*h*10	Sim	14	10.2	0.2	0.49	0.63	0.74
Densely vegetated *full* (*f*)	E*f*	Exp	28	1.2×10^{-2}	–	–	1.07	0.26
	S*f*1	Sim	28	1.2	0.2	4.14	1.09	0.28
	S*f*5	Sim	28	4.9	0.2	1.02	0.87	0.53
	S*f*10	Sim	28	10.2	0.2	0.49	0.63	0.74

Panel (b) reports the mean vertical velocity ($\overline{w}$). As expected, values are close to zero at the canyon center, reflecting the symmetry of the recirculation cell. A slightly positive vertical velocity is observed in the vegetated canyon, suggesting a mild asymmetry in the position of the recirculation cell. Differences among the three drag cases are minor.

Fig. 4.c presents the turbulent kinetic energy (k) profiles. In all configurations, k peaks in the rooftop shear layer and decreases sharply toward the canyon bottom. LES underestimates k in the canyon core: the reduction is about 30% in the empty case, and ranges from 20% to 40% in the vegetated canyon, depending on the applied drag length. This behavior is consistent with the boundary-layer results (Section 3.1): turbulence, already underestimated at $z/H \approx 1$, is further damped within the canyon. This stronger underestimation inside the canyon compared to the overlying boundary layer arises from the increased flow complexity within the canyon, including interacting shear layers and wall effects in the experiments, which are more difficult to fully resolve in LES. Systematic underprediction of turbulence in the roughness and canopy sublayer is well documented (Xie et al., 2004; Lim et al., 2009), typically attributed to limited resolution in high-shear regions, reduced lateral fluctuation levels, and wall models tuned to reproduce mean drag rather than turbulence intensities. Recent studies also indicate that mismatches in shear levels between LES and experiments can alter turbulence production and further contribute to k underestimation within the canopy layer (Teng et al., 2025; Mishra et al., 2025). Among the vegetated cases (blue lines in Fig. 4.c), the lowest drag ($\ell_d = 10$) provides the closest agreement, as weaker tree-induced damping partially compensates for the general LES underestimation of k.

4.2. Spatial structure of the mean velocity field

Fig. 5 shows the mean streamwise velocity ($\overline{u}$) along the canyon mid-plane ($x/H = 1$). Both wind tunnel data (a1, b1) and LES (a2–b4) capture the canonical recirculation cell, with positive velocities near rooftop and negative values near the ground. LES generally produces a thinner rooftop shear layer than the experiments, consistent with the reduced streamwise velocity at $z/H = 1$ seen in Fig. 2.a.

In the empty canyon, LES (Fig. 5.a2) reproduces the lateral variability observed in the wind tunnel (a1), with undulations along the canyon axis of wavelength $\sim 4H$. The position of velocity minima differs slightly between WT ($y/H \approx -1.5, 2$) and LES ($y/H \approx -3, 1$), indicating a lateral shift in the recirculation pattern. These lateral undulations are intrinsic to the canyon flow and are not expected to result from the

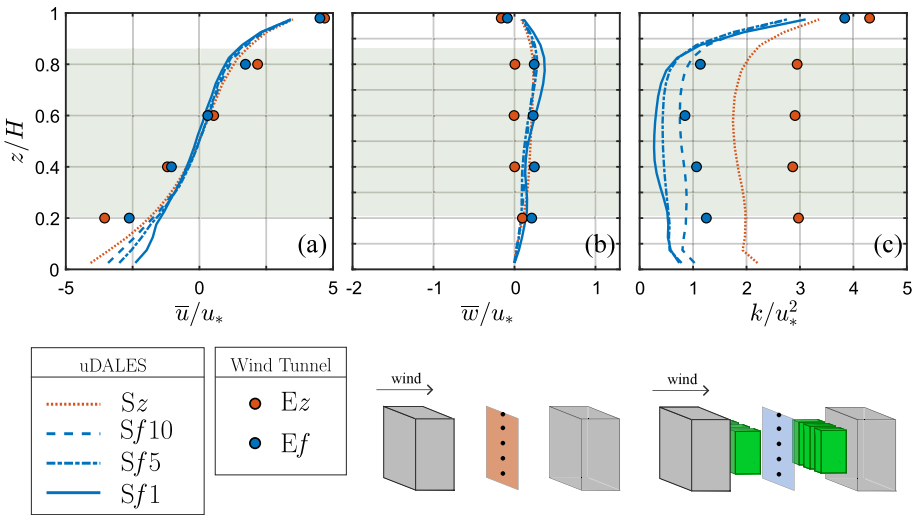

Fig. 4. Vertical profiles averaged over x and y of (a) mean horizontal velocity ($\overline{u}$), (b) mean vertical velocity ($\overline{w}$), and (c) turbulent kinetic energy (k) obtained in uDALES within the urban canyon. Orange refers to the empty canyon (*zero*) while blue refers to the densely vegetated one (*full*). Different markers and line styles correspond to different drag coefficients for the modeled trees. Circles denote the experimental point measurements taken at $x/H = 1$ and averaged along y. The green background in the graphs highlights the region occupied by tree crowns.

canyon being laterally closed, as previous work has shown that closed and effectively infinitely long canyons produce the same patterns in scalar fields (see Section 2.1). They also do not appear to depend on the lateral boundary conditions, as similar undulations are observed in both the wind tunnel (solid walls) and the LES (periodic boundaries), with a characteristic wavelength different from the domain width.

When vegetation is introduced (*full* configuration), the lateral variability is modulated by the tree spacing, as observed in both the wind tunnel (b1) and the LES (b2–b4). Increasing tree drag (low ℓ_d, b4) makes the undulations align with the tree positions (dashed lines), while for weaker drag (high ℓ_d, b2) the velocity field reflects two dominant scales: the canyon width and the tree spacing. This dual-scale interaction is also visible in the experiments, where neither scale fully dominates the flow pattern.

Fig. 6 shows the mean vertical velocity field ($\overline{w}$). In the empty canyon, both WT (a1) and LES (a2) reveal a periodic structure with wavelength ≈4H, consisting of alternating updraft and downdraft regions along the canyon axis. These updrafts coincide with zones where the shear layer at the canyon top thins, reflecting the continuity constraint: reduced streamwise velocity is compensated by upward motion to conserve mass.

When vegetation is introduced (*full* case, Fig. 6.b1–b4), the vertical velocity field becomes more homogeneous along the canyon axis, and the contrast between updraft and downdraft regions is reduced. Nevertheless, localized updrafts are still visible in both WT and LES. As the tree drag increases, the spacing between these updrafts becomes narrower and more regular, following the periodicity imposed by the tree arrangement. This trend is clearest in the high-drag case (b4), where vertical updrafts predominantly occur between the tree crowns above the canopy, while beneath the canopy, localized updrafts emerge directly beneath the tree locations. This apparent inversion — where vertical velocities increase at the tree positions rather than in the gaps — can be explained by the redistribution of momentum within the canopy layer. The high drag exerted by tree crowns significantly slows down the horizontal flow beneath the crowns (see $\overline{u}$ pattern in Fig. 5.b4), inducing local pressure build-up. This pressure gradient redirects part of the horizontal momentum into vertical motion, generating localized updrafts beneath the trees.

The streamlines in Fig. 7, obtained from uDALES simulations, complement the velocity fields shown in Figs. 5 and 6 by providing an integrated view of canyon-scale circulation. Streamlines were initialized at street level along the canyon centerline (yellow dots), allowing comparison between the empty canyon (Sz, panels a1–a3) and the densely vegetated case (Sf1, panels b1–b3).

In the empty canyon, a well-defined recirculation cell develops, organized along the canyon axis. Velocities peak near rooftop height, and air exits predominantly through three regions: one central and two at the lateral edges. Together with Figs. 5–6, these streamlines suggest that the flow field is structured into laterally converging and diverging recirculation cells, each of size of approximately 2H along both the x- and y-axes. The arrows in panel a2 indicate regions of lateral convergence and outflow, helping to visualize the organization of the recirculating cells.

In the *full* configuration, vegetation profoundly reshapes the flow. At street level (Fig. 7.b3), the flow is confined by the trees toward the central region of the canyon, with air reaching the upwind wall only through the gaps between trunks. Velocity magnitudes are strongly reduced compared to the empty canyon. The recirculating pattern, which in the tree-free case already consists of laterally converging and diverging cells, becomes further disrupted and segmented by the tree drag. Vegetation thus superimposes secondary spatial scales on the canyon circulation, reducing its coherence and altering the pathways through which ventilation occurs.

In addition to the in-canyon flow features, uDALES simulations also reveal spanwise variations in the boundary layer above the rooftops. Fig. 8 illustrates spanwise modulations of the mean streamwise velocity on a vertical plane at the canyon centerline ($x/H = 1$). Velocity profiles are extracted along horizontal lines at different heights ($z/H = 0.5$, 1, 1.5, 2, 2.5, and 3). For clarity, only two configurations are shown: Sz and Sf1.

Spanwise heterogeneity in rough-wall boundary layers has been widely documented in the literature (e.g., Perret and Savory, 2013; Perret et al., 2019; Reynolds and Castro, 2008; Vanderwel and Ganapathisubramani, 2015), beginning with Reynolds et al. (2007), who first identified secondary flows with characteristic wavelengths related to canopy geometry within the inertial sublayer.

Consistent with these studies, Fig. 8 shows spanwise periodicity governed by a length scale of about 6H, with velocity fluctuation amplitude decreasing with height. In the empty canyon (Fig. 8.a), these spanwise structures in the lower boundary layer couple with the canyon flow, producing internal spanwise variations with a wavelength of approximately 4H, reflecting the coupling between the overlying flow and the canyon geometry.

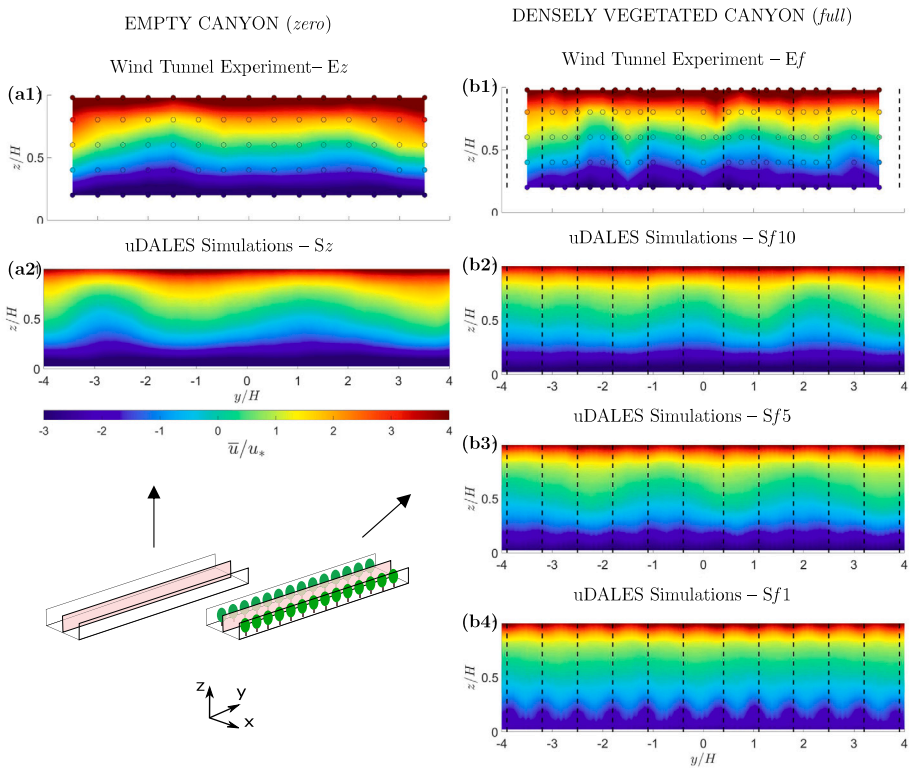

Fig. 5. Two-dimensional sections of mean horizontal velocity ($\overline{u}$) on the vertical plane at canyon centerline ($x/H = 1$). Wind Tunnel Experiment: (a1) empty canyon (*zero* - E*z*), (b1) densely vegetated canyon (*full* - E*f*); circles indicate measurement points. uDALES Simulations: (a2) empty canyon (*zero* - S*z*); (b2–b4) densely vegetated canyon (*full* - S*f*) with decreasing ℓ_d (increasing C_d). Bottom-left sketch: location of the section plane.

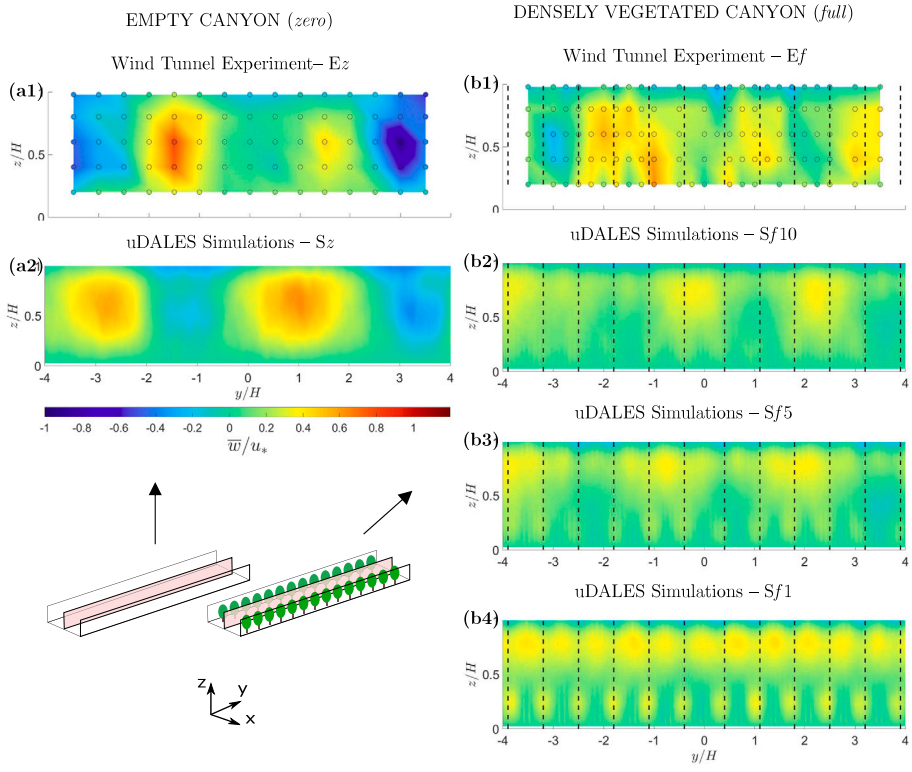

Fig. 6. Two-dimensional sections of mean vertical velocity ($\overline{w}$) on the vertical plane at canyon centerline ($x/H = 1$). Wind Tunnel Experiment: (a1) empty canyon (*zero* - E*z*), (b1) densely vegetated canyon (*full* - E*f*); circles indicate measurement points. uDALES Simulations: (a2) empty canyon (*zero* - S*z*); (b2–b4) densely vegetated canyon (*full* - S*f*) with decreasing ℓ_d (increasing C_d). Bottom-left sketch: location of the section plane.

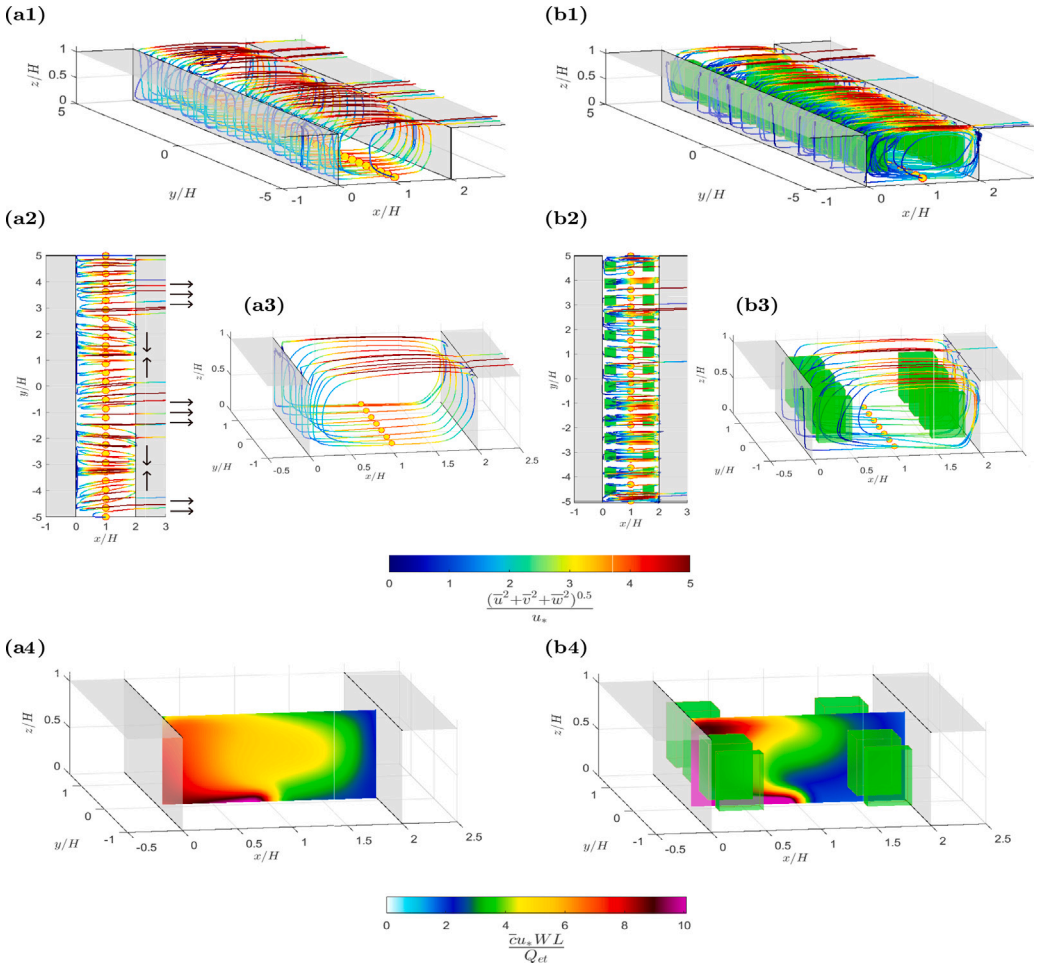

Fig. 7. uDALES simulations for the empty canyon (*zero*, Sz, left) and the densely vegetated canyon (*full*) with high tree drag (*Sf*1, right). (a1–b1) Streamlines of the velocity field, colored by velocity magnitude. (a2–b2) Top view of the streamlines, with arrows indicating regions of lateral convergence and outflow. (a3–b3) Streamlines in the core of the canyon. (a4–b4) Time-averaged pollutant concentration on the vertical plane at $y/H = 1$.

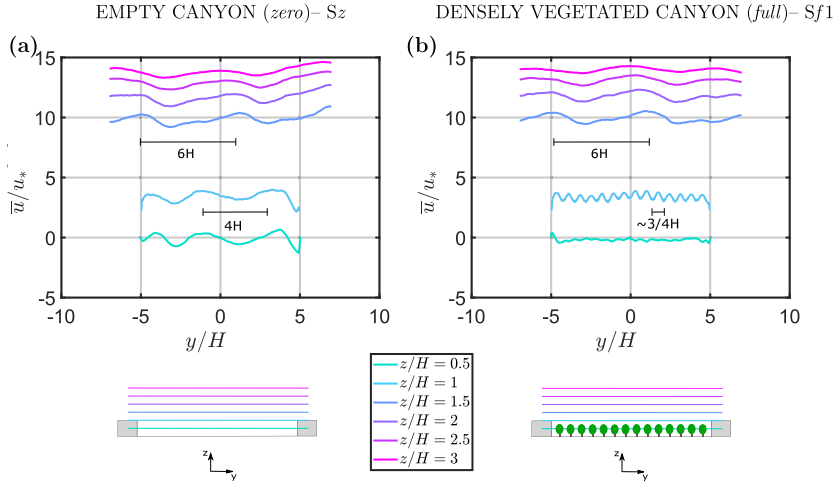

Fig. 8. Spanwise profiles of mean streamwise velocity $\overline{u}/u_*$ at different heights (z/H = 0.5, 1, 1.5, 2, 2.5, 3) along a vertical plane at the canyon centerline (x/H = 1). Panel (a) shows the empty canyon configuration (Sz), while panel (b) corresponds to the densely vegetated case (*Sf*1), with maximum vegetation drag. The characteristic wavelengths of the spanwise velocity variations are indicated: about 6H above the canopy, 4H inside the empty canyon, and 3/4H inside the vegetated canyon.

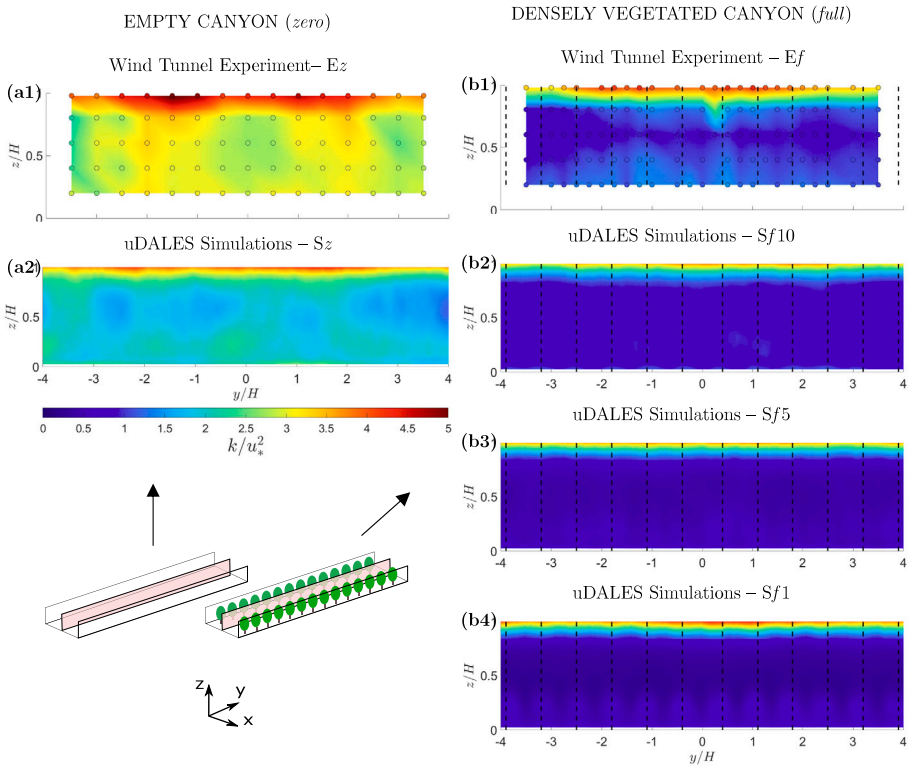

Fig. 9. Two-dimensional sections of turbulent kinetic energy (k) on the vertical plane at canyon centerline ($x/H = 1$). Wind Tunnel Experiment: (a1) empty canyon (*zero* - Ez), (b1) densely vegetated canyon (*full* - Ef); circles indicate measurement points. uDALES Simulations: (a2) empty canyon (*zero* - Sz); (b2–b4) densely vegetated canyon (*full* - Sf) with decreasing ℓ_d (increasing C_d). Bottom-left sketch: location of the section plane.

In the densely vegetated canyon (Fig. 8.b), the amplitude of spanwise fluctuations is markedly reduced. Vegetation thus damps large-scale spanwise structures while introducing additional periodicity with a shorter wavelength of ~3/4H, comparable to the tree spacing, further modifying the three-dimensional flow within the canyon.

4.3. Turbulent kinetic energy inside the canyon

To conclude the analysis of the flow field within the canyon, Fig. 9 presents the turbulent kinetic energy (k) in the central spanwise–vertical plane of the canyon. In all configurations, k reaches significantly higher values in the shear layer at rooftop height ($z = H$) compared to the canyon interior: approximately twice as large in the empty canyon and up to five times greater in the densely vegetated case.

In the absence of trees (left panels), turbulence generated in the shear layer penetrates into the canyon, as expected for a wake-interference regime (Oke, 1988), typically associated with aspect ratios $W/H > 1.5$. In contrast, the flow in the vegetated canyon behaves more like a skimming-flow regime (Oke, 1988), with a partial decoupling between the turbulent eddies above and those inside the canyon (Salizzoni et al., 2011; Marucci and Carpentieri, 2019; Fellini et al., 2020).

Consistently with the boundary-layer analysis (Fig. 2) and the results shown in Fig. 4, LES underestimates k at rooftop height ($z/H \approx 1$); combined with the challenges of resolving wall-generated turbulence inside the canyon, this leads to weaker turbulence levels compared to the experiments. Averaging k over the cross-sections shown in Fig. 9 confirms this tendency: LES underestimates k by about 38% in the empty canyon, and by 40%–57% in the vegetated cases, with the discrepancy increasing as tree drag strengthens. Within the vegetated canyon, increasing drag produces a clear fingerprint in the k field, characterized by spatially heterogeneous damping of turbulence throughout the volume. Among the tested drag scenarios, the lowest drag length ($\ell_d = 10$ m) yields the closest match with wind tunnel measurements, as the weaker damping partly compensates for the general underestimation of turbulent kinetic energy by LES.

4.4. Spatial distribution of pollutant concentrations

Figs. 10 and 11 compare mean pollutant concentration fields on vertical cross-sections at different streamwise locations (x/H) within the canyon. Concentrations are expressed in nondimensional form as

$$\overline{c}^* = \frac{\overline{c} u_* W L}{Q_{et}}, \tag{10}$$

where u_* is the friction velocity of the approaching boundary layer, W and L are the width and length of the canyon, and Q_{et} is the ethane mass flow rate [g/s]. This non-dimensionalization is derived from the pollutant mass balance over the canyon control volume (see the Appendix for details). In this framework, the average canyon concentration scales as $Q_{et}/(u_d\, W\, L)$, where u_d is a bulk vertical exchange velocity at roof level (see Section 4.6). Since u_d is driven by turbulent transport near the canyon top, it is natural to scale it — and thus concentration — with the friction velocity u_*, which characterizes the momentum and turbulence input from the boundary layer. As discussed in Section 3.1, u_* provides a more robust scaling than the free-stream velocity U_∞, especially in a fully developed boundary layer such as in LES, where U_∞ is not well defined. Using u_* as the velocity scale therefore ensures consistency between the two setups and captures the dominant physical mechanisms driving pollutant transport.

Fig. 10 compares the experimental data (left panels, configuration Ez) and uDALES simulations (right panels, Sz) for the empty canyon.

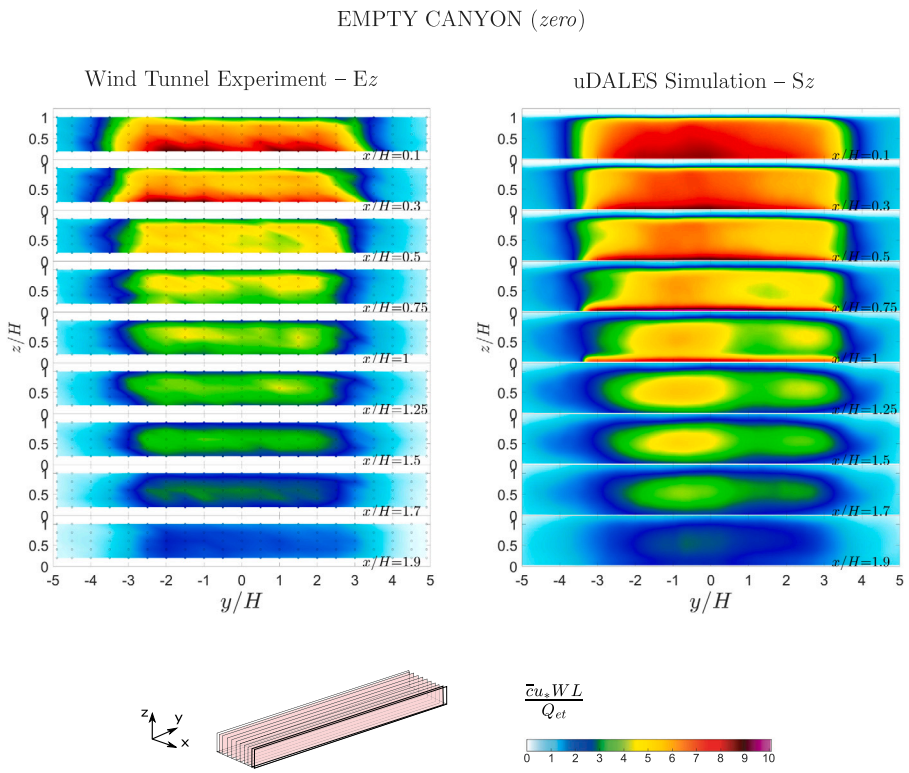

Fig. 10. Mean normalized concentration fields ($\overline{c}^*$) on vertical cross-sections at various streamwise positions (x/H) within the empty canyon (*zero*) configuration. Left: wind tunnel measurements (E*z*) with circles representing the measuring points; right: uDALES simulations (S*z*).

Each row corresponds to a vertical y–z cross-section at a given streamwise location, from the upwind wall ($x/H = 0.1$) to the downwind wall ($x/H = 1.9$).

Both datasets display the characteristic pattern of street canyons with perpendicular wind and a central line source (e.g., Fellini et al., 2020; Bazdidi-Tehrani et al., 2023): concentrations are lowest near the downwind wall, where clean air entrains from above, and increase toward the upwind wall due to accumulation. This streamwise gradient is also evident in panel a4 of Fig. 7, which shows a vertical cross-section aligned with the wind direction at $y/H = 0$.

The influence of the finite source extent along y is also clear: for $|y/H| > 3.25$ concentrations drop sharply outside the emission zone, while within it they remain fairly homogeneous. Finally, LES capture the sharp near-ground concentration peak ($z \to 0$), directly linked to the source location. This region, corresponding to pedestrian level, is difficult to resolve in wind-tunnel experiments—highlighting the added value of LES in quantifying near-wall pollutant transport in complex geometries.

Fig. 11 presents the concentration fields for the densely vegetated canyon. As with the velocity analysis, experimental results (E*f*, left column) are compared with uDALES simulations for three vegetation drag lengths: Sf10, Sf5, and Sf1. Vertical dashed lines mark the positions of the tree trunks along the y-axis. In the experimental data, the concentration field exhibits two nearly symmetric accumulation zones (located at $|y/H| \approx 2$) and a clear low-concentration region around the canyon center ($y/H \approx 0$) (Fellini et al., 2022; Del Ponte et al., 2024). Here, the average concentration is approximately half that measured in the accumulation zones. This pattern persists across all x/H locations, suggesting that it arises from the overall impact of vegetation on canyon-scale recirculation rather than from the exact placement of individual trees.

Compared to the empty canyon (Fig. 10), the vegetated configuration exhibits a steeper concentration gradient along the x-axis: pollutant levels increase near the upwind wall, while remaining nearly unchanged at the downwind wall. This behavior is consistent with previous findings (e.g., Gromke et al., 2008; Buccolieri et al., 2009), which reported enhanced accumulation near the upwind wall due to vegetation-induced flow modifications.

The LES reproduce these overall trends, but the degree of spanwise heterogeneity depends strongly on the drag parameterization. In the low-drag case (Sf10), the concentration field is relatively smooth, similar to the empty canyon. With intermediate drag (Sf5), accumulation zones appear more distinct, although still less sharply than in the experiments. With high drag (Sf1), strong spanwise modulation emerges, with alternating high- and low-concentration bands aligned with the tree positions. Since these features are absent in the experimental data, this suggests that Sf1 overestimates the tree drag, producing excessive confinement and artificial compartmentalization of the scalar field.

The comparison between panels a4 and b4 of Fig. 7 confirms the different spatial distribution of pollutants in the vegetated canyon (Sf1) with respect to the empty one (S*z*), with a clear confinement of the pollutant near the upwind wall and a noticeable decrease in concentration toward the downwind wall.

4.5. Vertical scalar fluxes across the canyon roof

Figs. 12 and 13 show the vertical pollutant fluxes at rooftop level ($z/H = 1$), separating the mean contribution $\overline{w}\,\overline{c}$ from the turbulent term $\overline{w'c'}$. Analyzing these fluxes is essential to understand the vertical exchange between the street canyon and the overlying boundary layer. Minor numerical oscillations visible in the LES fields (Figs. 12 and 13) are artifacts of the central-difference discretization scheme.

In the non-vegetated canyon, experiments (Fig. 12.a1) show the expected pattern: negative fluxes near the downwind wall, where clean air enters, and positive fluxes near the upwind wall, where polluted

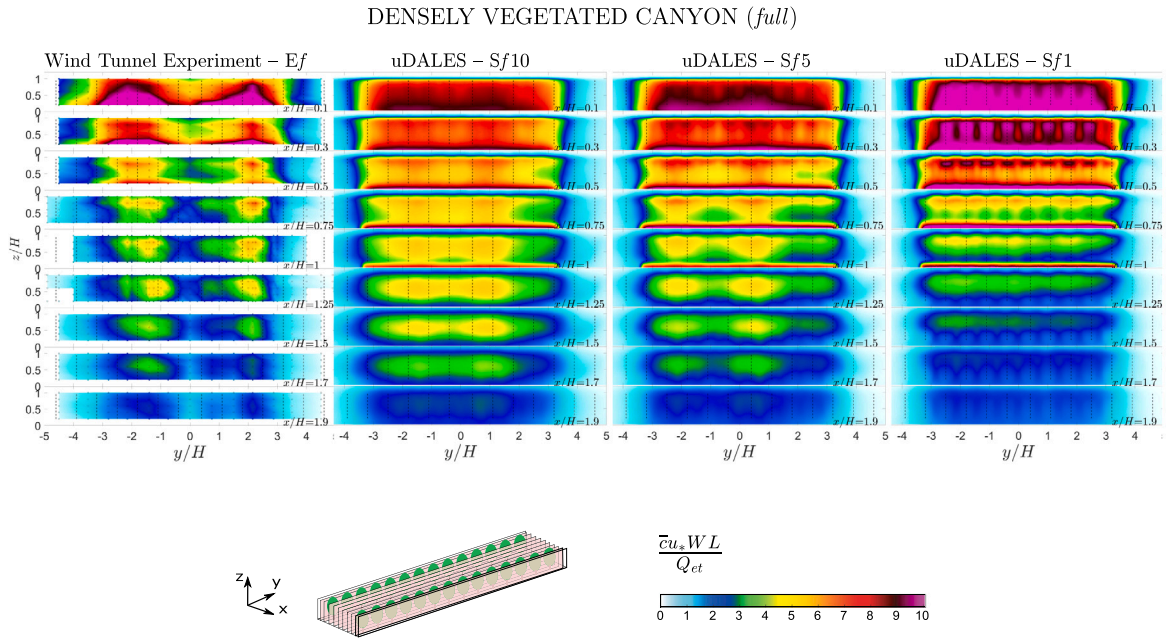

Fig. 11. Mean normalized concentration fields ($\overline{c}^*$) on vertical cross-sections at various streamwise positions (x/H) within the densely vegetated (*full*) canyon. Left: wind tunnel experiment (E*f*), with circles indicating the measurement points. Right three columns: uDALES simulations with increasing vegetation drag, from $\ell_d = 10.2$ (S*f*10), to $\ell_d = 4.9$ (S*f*5), and $\ell_d = 1{-}2$ (S*f*1). Vertical dashed lines denote the positions of trees along the spanwise direction (y-axis).

air is expelled. uDALES (Fig. 12.a2) reproduces both magnitude and spatial distribution, and further resolves near-wall regions of intensified exchange. Weak spanwise oscillations, consistent with the vertical velocity field (Fig. 6), are captured in both setups.

In the vegetated canyon, $\overline{w}\,\overline{c}$ becomes strongly modulated along y. Experiments (Fig. 12.b1) display alternating zones of upward and downward fluxes, linked to tree spacing. LES reproduces this footprint, though with increasing fragmentation as vegetation drag increases: from S*f*10 to S*f*1, upward fluxes are progressively confined to the inter-tree gaps, while tree locations act as barriers. This spatial fragmentation reflects the influence of trees on scalar exchange and suggests that vegetation not only modifies recirculation within the canyon but also channels the upward pollutant transport through localized vertical corridors.

Fig. 13 complements this analysis by presenting the turbulent component of the vertical mass flux, $\overline{w'c'}$. In all configurations, the flux is positive, confirming the consistent role of turbulence in transporting pollutants upward. LES data closely match the experimental trend, capturing the relatively homogeneous distribution.

In the empty canyon, LES fluxes (Fig. 13.a2) are lower than the experimental values (a1), with a reduction of approximately 25%. This behavior is consistent with the underestimation of turbulent kinetic energy in the rooftop shear layer discussed in Section 3.1. The reduced turbulent energy weakens vertical mixing efficiency, resulting in noticeably lower $\overline{w'c'}$ in the simulations.

In the vegetated canyon, the experimental data (Fig. 13.b1) show an enhancement of turbulent mass flux, with average values at roof level increasing by about 20% compared to the empty canyon. In contrast, LES results show no such enhancement: average values remain nearly unchanged and even decrease slightly (by about 1%–2%) as vegetation drag increases from S*f*10 to S*f*1. This suggests that while the wind tunnel captures a modest roof-level enhancement, likely linked to canopy–shear layer interactions, the simulations do not reproduce this effect and instead yield nearly constant fluxes across vegetation scenarios.

4.6. Canyon ventilation

Pollutant ventilation in street canyons plays a central role in determining urban air quality. A commonly used indicator of ventilation efficiency is the vertical bulk exchange velocity, u_d (Salizzoni et al., 2009; Soulhac et al., 2011; Kim et al., 2018), which quantifies the effective rate at which pollutants are removed from the canyon volume and transported to the overlying atmosphere. Larger values of u_d indicate more efficient pollutant removal. This parameter is also widely used in operational urban air quality models, where it controls pollutant propagation and dilution at the neighborhood scale (Soulhac et al., 2011; Fellini et al., 2021).

The vertical bulk exchange velocity (u_d) can be directly derived from the pollutant mass balance within the street canyon, as detailed in the Appendix:

$$u_d = \frac{Q_{et}}{C_{vol} W L} \tag{11}$$

where C_{vol} is the pollutant concentration averaged in the canyon volume, Q_{et} is the mass flow rate of ethane at the source, the product $W\,L$ provides the area of the canyon boundary surface at the roof height.

Table 2 compares the uDALES-based estimates of u_d (from Eq. (11)) with wind tunnel values from Fellini et al. (2022). In all cases, LES predictions of u_d/u_* are lower than the experimental values. This discrepancy is consistent with the higher pollutant concentrations observed in LES (Figs. 10–11), especially near the source region, at pedestrian level, and along the upwind wall—areas that are particularly difficult to probe in the wind tunnel. Part of this lower exchange efficiency may be related to the underestimation of turbulent kinetic energy in the LES, which reduces turbulent mixing and the vertical transport of pollutants within the canyon.

Nevertheless, the uDALES simulations reproduce the overall experimental trend, showing no systematic variation in exchange velocity with increasing tree density. This contrasts with the results of Grylls and van Reeuwijk (2022), who reported a systematic decrease in u_d when

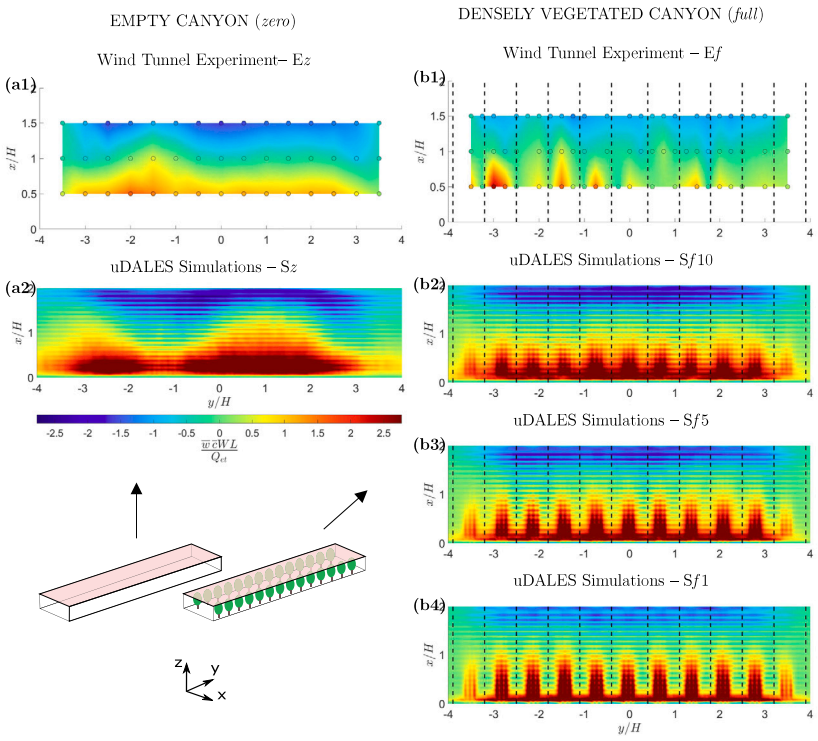

Fig. 12. Two-dimensional sections of mean vertical mass fluxes ($\overline{wc}$) at the canyon roof ($z/H = 1$). Wind Tunnel Experiment: (a1) empty canyon (*zero* - Ez), (b1) densely vegetated canyon (*full* - E*f*); circles indicate measurement points. uDALES Simulations: (a2) empty canyon (*zero* - Sz); (b2–b4) densely vegetated canyon (*full* - S*f*) with decreasing ℓ_d (increasing C_d). Bottom-left sketch: location of the section plane.

Table 2
Comparison of the vertical exchange velocity u_d/u_* obtained from wind tunnel experiments and uDALES simulations (source-based method, Eq. (11)). For vegetated configurations, uDALES results are shown for different drag lengths ℓ_d and corresponding drag coefficients C_d.

Configuration	Exp	uDALES simulations			
	$C_d = 1.07$	$\ell_d \to \infty$ m $C_d = 0$	$\ell_d = 10.2$ m $C_d = 0.63$	$\ell_d = 4.9$ m $C_d = 0.87$	$\ell_d = 1.21$ m $C_d = 1.09$
Empty (*zero*)	(Ez) 0.43	(Sz) 0.30	–	–	–
Sparsely vegetated (*half*)	(E*h*) 0.37	–	(S*h*10) 0.29	(S*h*5) 0.30	(S*h*1) 0.30
Densely vegetated (*full*)	(E*f*) 0.40	–	(S*f*10) 0.30	(S*f*5) 0.31	(S*f*1) 0.30

trees were added to a canyon. The discrepancy can be explained by key differences between the two studies: (1) their canyon had an aspect ratio of $H/W = 1$, compared to $H/W = 0.5$ here; (2) vegetation was represented as idealized 2D hedgerows, whereas in the present work trees are resolved with a three-dimensional geometry; (3) their vegetation occupied about 75% of the canyon plan area, versus a maximum of 28% in the present setup. These differences highlight that the impact of vegetation on canyon ventilation depends not only on its overall density, but also on its spatial arrangement and three-dimensional structure. Additionally, Table 2 shows negligible differences in u_d/u_* across the various drag length configurations (ℓ_d), despite the clear influence of vegetation drag on the spatial distribution of pollutants. This suggests that while tree-induced drag strongly modulates local concentration patterns within the canyon, it has a limited impact on the volume-averaged concentration, and thus on the overall exchange velocity.

An alternative method for computing u_d directly from the vertical mass fluxes at roof level in uDALES is presented in the Appendix and compared with the values discussed here.

5. Conclusions

This study addressed a topic of high relevance for the development of green solutions in urban areas: the impact of trees on airflow, pollutant dispersion, and ventilation efficiency in street canyons. To investigate this, we compared high-resolution wind tunnel experiments with Large-Eddy Simulations (LES) performed using uDALES, thereby gaining new insights into the role of trees in modulating canyon ventilation and identifying key considerations for relating numerical simulations to laboratory measurements in vegetated urban environments.

The analysis of the boundary layer above the canopy highlighted the importance of using the friction velocity (u_*) and the building geometry (H) as reference scales for comparing velocity and scalar fields. Because experimental and numerical boundary layers are generated through fundamentally different procedures, their vertical structure cannot be expected to match exactly. What is essential, however, is that the portion of the boundary layer governing canyon–atmosphere exchange is consistent across the two approaches. In this respect, u_* captures the dynamic forcing that drives ventilation processes, while H reflects the geometric confinement of the canyon. Beyond its role in momentum scaling, u_* also provided a coherent velocity reference

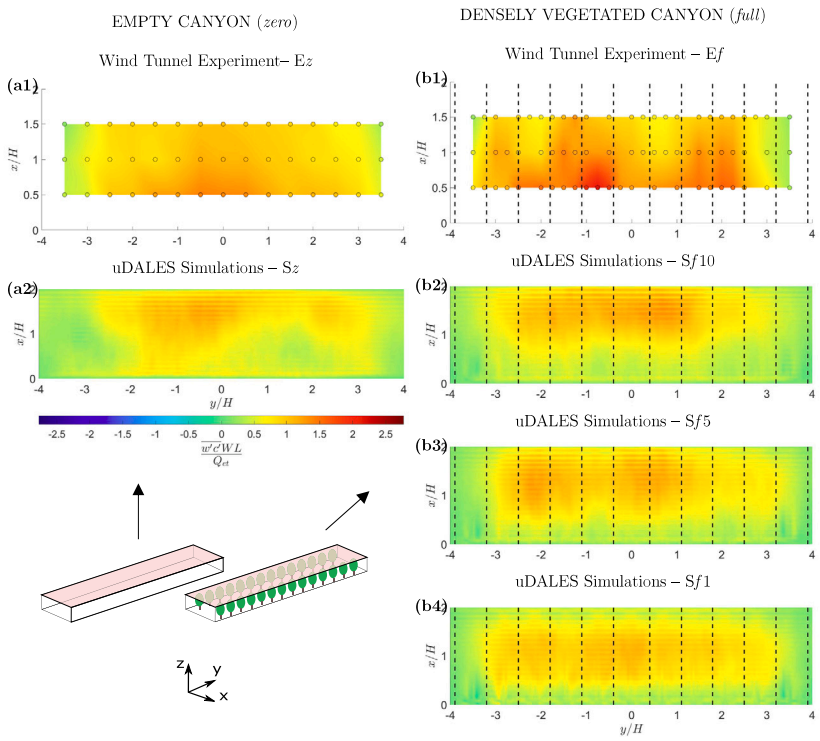

Fig. 13. Two-dimensional sections of turbulent vertical mass fluxes ($\overline{w'c'}$) at the canyon roof ($z/H = 1$). Wind Tunnel Experiment: (a1) empty canyon (*zero* - Ez), (b1) densely vegetated canyon (*full* - Ef); circles indicate measurement points. uDALES Simulations: (a2) empty canyon (*zero* - Sz); (b2–b4) densely vegetated canyon (*full* - Sf) with decreasing ℓ_d (increasing C_d). Bottom-left sketch: location of the section plane.

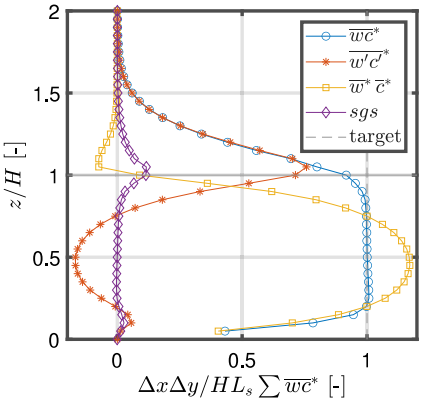

Fig. A.14. Vertical profiles of normalized concentration fluxes for configuration Sz. Solid blue: total scalar flux ($\overline{wc}^*$); dashed orange: mean advective flux ($\overline{w}^*\,\overline{c}^*$); dotted yellow: turbulent flux ($\overline{w'c'}^*$); dash-dotted purple: subgrid-scale flux. The vertical dashed black line denotes the target flux corresponding to the source strength.

for pollutant concentration and ventilation metrics, such as the bulk exchange velocity u_d.

Tree drag length (ℓ_d) was identified as a crucial parameter for aligning the aerodynamic resistance of simulated trees with experimental measurements. However, even when drag was tuned, the model did not fully reproduce the canyon velocity and dispersion fields: better agreement was obtained with reduced drag, likely because LES underestimates turbulent kinetic energy in the empty canyon and the lower tree drag partly compensates for this deficiency. The simplified cuboid representation of trees in LES, compared to the realistic morphologies of the wind tunnel, also likely contributed to discrepancies in the scalar fields.

The simulations revealed secondary flow structures in the boundary layer and their extension into the canyon. Vegetation introduced an additional length scale that modified the flow topology: with increasing tree density, the velocity field became more uniform along the canyon axis, while pollutant concentrations developed marked spanwise variability. These effects, though apparently contradictory, can be reconciled by considering the vegetation-induced reduction in turbulent kinetic energy and scalar fluxes, which reduces mixing efficiency and enhances concentration heterogeneity.

A central novelty of this work was the unprecedented comparison of mean and turbulent mass fluxes at the canyon roof. LES captured the dominant ventilation mechanisms, and the bulk vertical exchange velocity (u_d) showed no systematic dependence on tree number or drag intensity. This outcome, while specific to the studied configuration (perpendicular wind, $H/W = 0.5$, lateral tree placement), differs from previous studies and highlights the strong sensitivity of ventilation metrics to flow configuration, vegetation representation, and boundary-layer forcing.

In conclusion, this study highlights both the potential and the limitations of LES in representing the complex interactions between turbulent flow, vegetation, and pollutant transport in street canyons. While LES underestimates turbulent kinetic energy, particularly near the canyon roof and within the canyon core, which affects turbulent mixing, vertical mass fluxes, and the bulk exchange velocity u_d, the simulations nonetheless reproduce the mean flow and concentration fields as well as the key ventilation mechanisms observed in the wind tunnel. Further work is needed to advance vegetation representation, especially regarding morphological complexity and scalar dispersion, and to improve the treatment of near-wall turbulence processes that govern canyon ventilation. At the same time, high-resolution wind-tunnel experiments remain indispensable as the benchmark for model evaluation. Ultimately, the integration of synchronized experiments and LES establishes a cross-methodological framework that leverages the strengths of both approaches and advances urban microclimate and air quality modeling.

Table A.3
Comparison of the vertical exchange velocity u_d/u_* obtained from wind tunnel experiments and uDALES simulations (flux-based method, Eq. (A.3)). For vegetated configurations, uDALES results are shown for different drag lengths ℓ_d and corresponding drag coefficients C_d.

Configuration	Exp	uDALES simulations			
	$C_d = 1.07$	$\ell_d \to \infty$ m $C_d = 0$	$\ell_d = 10.2$ m $C_d = 0.63$	$\ell_d = 4.9$ m $C_d = 0.87$	$\ell_d = 1.21$ m $C_d = 1.09$
Empty (*zero*)	(Ez) 0.43	(Sz) 0.27	–	–	–
Sparsely vegetated (*half*)	(E*h*) 0.37	–	(S*h*10) 0.26	(S*h*5) 0.27	(S*h*1) 0.27
Densely vegetated (*full*)	(E*f*) 0.40	–	(S*f*10) 0.27	(S*f*5) 0.28	(S*f*1) 0.27

CRediT authorship contribution statement

Sofia Fellini: Writing – review & editing, Writing – original draft, Visualization, Methodology, Formal analysis, Conceptualization. **Dipanjan Majumdar:** Writing – review & editing, Writing – original draft, Visualization, Methodology, Formal analysis, Conceptualization. **Pietro Salizzoni:** Writing – review & editing, Supervision, Methodology, Funding acquisition, Conceptualization. **Maarten van Reeuwijk:** Writing – review & editing, Supervision, Methodology, Funding acquisition, Conceptualization.

Declaration of competing interest

The authors declare that they have no known competing financial interests or personal relationships that could have appeared to influence the work reported in this paper.

Acknowledgments

SF acknowledges support from the Roberto Revelli Memorial Grant (DIATI–Politecnico di Torino). PS acknowledges funding from Region Auvergne Rhône Alpes through the VEB_{MU} project. DM and MvR acknowledges financial support through the Turbulence at the Exascale project (EP/W026686/1) which is part of the ExCALIBUR HPC programme funded by EPSRC, United Kingdom. MvR also acknowledges the NERC Highlight project ASSURE: Across-Scale ProcesseS in Urban Environment (NE/W002868/1).

Appendix. Analysis of scalar flux balance and ventilation diagnostics

The vertical bulk exchange velocity can be directly related to the pollutant mass balance within the canyon. A street canyon can be conceptualized as a control volume characterized by a volume-averaged concentration C_{vol} and scalar fluxes across the boundary surfaces at the roof height (with an area of $L\,W$) and at the lateral edges (two rectangles with an area of $H\,W$). The general mass balance for this volume is expressed as:

$$V\frac{\mathrm{d}C_{vol}}{\mathrm{d}t}+\int_{-L/2}^{L/2}\int_{0}^{W}\left[\overline{wc}\right]_{z=H}\mathrm{d}x\,\mathrm{d}y+\int_{0}^{H}\int_{0}^{W}\left[\overline{vc}\right]_{y=0}^{y=L}\mathrm{d}x\,\mathrm{d}z=Q_{et},\quad(\text{A.1})$$

where V represents the volume of the canyon, Q_{et} is the mass flow rate of ethane at the source, and $\overline{wc}$ and $\overline{vc}$ denote the mass fluxes of the passive scalar in the vertical and longitudinal directions, respectively.

Assuming steady-state conditions ($\mathrm{d}C_{vol}/\mathrm{d}t = 0$) and impermeable lateral boundaries ($\overline{vc} = 0$), the balance simplifies to:

$$\int_{-L/2}^{L/2}\int_{0}^{W}\left[\overline{wc}\right]_{z=H}\mathrm{d}x\,\mathrm{d}y=Q_{et}.\quad(\text{A.2})$$

Following Salizzoni et al. (2009) and Soulhac et al. (2013), the net vertical flux at the rooftop can be written as the product of the bulk exchange velocity (u_d) and the concentration difference between the canyon and the external flow (C_{ext}):

$$u_d(C_{vol}-C_{ext})W\,L=\int_{-L/2}^{L/2}\int_{0}^{W}\left[\overline{wc}\right]_{z=H}\mathrm{d}y\,\mathrm{d}x.\quad(\text{A.3})$$

Given that $C_{vol} \gg C_{ext}$ in typical urban conditions, the external concentration is often neglected, yielding Eq. (11).

Eqs. (11) and (A.3) offer two alternative methods to estimate u_d from experimental or numerical data. The first is based on the ratio between the known source emission rate and the volume-averaged canyon concentration, while the second relies on direct integration of the vertical scalar flux across the rooftop.

The flux-based estimate of u_d was computed by integrating the net vertical scalar flux $\overline{wc}$ at the rooftop (Eq. (A.3)). Although this method is theoretically equivalent to the source-based formulation (Section 4.6), the resulting estimates in Table A.3 show that the flux-based values of u_d/u_* are consistently 8%–12% lower than those obtained with the source-based approach (Table 2) across all configurations. This systematic discrepancy highlights an imbalance between the pollutant flux injected into the domain and the net flux measured at the rooftop in the simulation.

To further investigate this imbalance, Fig. A.14 presents vertical profiles of the scalar flux components for configuration Sz, derived by integrating the normalized vertical fluxes across horizontal planes at varying elevations z. The total vertical scalar flux ($\overline{wc}^*$) does not fully align with the injected flux, particularly at the rooftop level ($z/H = 1$). The turbulent flux component ($\overline{w'c'}^*$) is notably underestimated within the shear layer, while the subgrid-scale (sgs) flux provides only partial compensation. This indicates that both mesh resolution and subgrid modeling limit the accurate representation of turbulent transport processes in this region. Moreover, possible leakage of scalar (through the building surfaces) associated with the implementation of immersed boundary method in uDALES (Suter et al., 2021) may be one reason behind this error. On the other hand, discrepancies in the flux balance observed near the ground can be attributed to the scalar emission being modeled as a volumetric source distributed over several grid cells (see Section 2.2). This spread influences the local scalar fluxes and contributes to the overall imbalance near the ground.

In light of these findings, the source-based approach provides a reliable and consistent framework for estimating u_d in LES studies, as it directly reflects the known pollutant input and captures the global ventilation dynamics within the canyon. While the flux-based method offers valuable diagnostic insights, revealing local imbalances in scalar fluxes at the rooftop, these discrepancies are inherent to the numerical resolution and subgrid-scale modeling adopted in LES. Such differences highlight the complexity of turbulent transport at fine scales and suggest avenues for further refinement, particularly in resolving rooftop fluxes and enhancing subgrid representations.

Data availability

The experimental dataset (Fellini et al., 2025) is available at: https://zenodo.org/records/15633150. We provide concentration, velocity, and turbulent mass fluxes data within the canyon, and the characterization of the flow field above the buildings.

References

Abhijith, K., Kumar, P., Gallagher, J., McNabola, A., Baldauf, R., Pilla, F., Broderick, B., Di Sabatino, S., Pulvirenti, B., 2017. Air pollution abatement performances of green infrastructure in open road and built-up street canyon environments–a review. Atmos. Environ. 162, 71–86.

Allegrini, J., Dorer, V., Carmeliet, J., 2013. Wind tunnel measurements of buoyant flows in street canyons. Build. Environ. 59, 315–326.

Auvinen, M., Boi, S., Hellsten, A., Tanhuanpää, T., Järvi, L., 2020. Study of realistic urban boundary layer turbulence with high-resolution large-eddy simulation. Atmosphere 11, 201.

Bazdidi-Tehrani, F., Bodaghi, D., Kiamansouri, M., 2023. Large eddy simulation of flow and pollutant dispersion in a street canyon: analysis of performance of various inflow turbulence generation techniques. Environ. Fluid Mech. 23, 1283–1312.

Blunn, L.P., Coceal, O., Nazarian, N., Barlow, J.F., Plant, R.S., Bohnenstengel, S.I., Lean, H.W., 2022. Turbulence characteristics across a range of idealized urban canopy geometries. Bound.-Layer Meteorol. 182, 275–307.

Buccolieri, R., Gromke, C., Di Sabatino, S., Ruck, B., 2009. Aerodynamic effects of trees on pollutant concentration in street canyons. Sci. Total Environ. 407, 5247–5256.

Buccolieri, R., Salim, S.M., Leo, L.S., Di Sabatino, S., Chan, A., Ielpo, P., de Gennaro, G., Gromke, C., 2011. Analysis of local scale tree–atmosphere interaction on pollutant concentration in idealized street canyons and application to a real urban junction. Atmos. Environ. 45, 1702–1713.

Buccolieri, R., Santiago, J.L., Rivas, E., Sanchez, B., 2018. Review on urban tree modelling in cfd simulations: Aerodynamic, deposition and thermal effects. Urban For. Urban Green. 31, 212–220.

Busca, F., Revelli, R., 2022. Green areas and climate change adaptation in a urban environment: The case study of Le Vallere Park (Turin, Italy). Sustainability 14, 8091.

Chatzimichailidis, A.E., Argyropoulos, C.D., Assael, M.J., Kakosimos, K.E., 2019. Qualitative and quantitative investigation of multiple large eddy simulation aspects for pollutant dispersion in street canyons using openfoam. Atmosphere 10, 17.

Dai, Y., Basu, S., Maronga, B., de Roode, S.R., 2021. Addressing the grid-size sensitivity issue in large-eddy simulations of stable boundary layers. Bound.-Layer Meteorol. 178, 63–89.

Deardorff, J.W., 1980. Stratocumulus-capped mixed layers derived from a three-dimensional model. Bound.-Layer Meteorol. 18, 495–527.

Del Ponte, A.V., Fellini, S., Marro, M., van Reeuwijk, M., Ridolfi, L., Salizzoni, P., 2024. Influence of street trees on turbulent fluctuations and transport processes in an urban canyon: a wind tunnel study. Bound.-Layer Meteorol. 190, 6.

Fellini, S., Del Ponte, A.V., Marro, M., Salizzoni, P., Ridolfi, L., 2025. Wind tunnel measurements of concentration and velocity in urban geometries with trees. http://dx.doi.org/10.5281/zenodo.15633150.

Fellini, S., Marro, M., Del Ponte, A.V., Barulli, M., Soulhac, L., Ridolfi, L., Salizzoni, P., 2022. High resolution wind-tunnel investigation about the effect of street trees on pollutant concentration and street canyon ventilation. Build. Environ. 226, 109763.

Fellini, S., Ridolfi, L., Salizzoni, P., 2020. Street canyon ventilation: Combined effect of cross-section geometry and wall heating. Q. J. R. Meteorol. Soc..

Fellini, S., Salizzoni, P., Ridolfi, L., 2021. Vulnerability of cities to toxic airborne releases is written in their topology. Sci. Rep. 11, 23029.

Finnigan, J., 2000. Turbulence in plant canopies. Annu. Rev. Fluid Mech. 32, 519–571.

Fu, R., Paden, I., García-Sánchez, C., 2024. Should we care about the level of detail in trees when running urban microscale simulations? Sustain. Cities Soc. 101, 105143.

Gromke, C., 2011. A vegetation modeling concept for building and environmental aerodynamics wind tunnel tests and its application in pollutant dispersion studies. Environ. Pollut. 159, 2094–2099.

Gromke, C., Buccolieri, R., Di Sabatino, S., Ruck, B., 2008. Dispersion study in a street canyon with tree planting by means of wind tunnel and numerical investigations–evaluation of cfd data with experimental data. Atmos. Environ. 42, 8640–8650.

Grylls, T., van Reeuwijk, M., 2021. Tree model with drag, transpiration, shading and deposition: Identification of cooling regimes and large-eddy simulation. Agricult. Forest. Meterol. 298, 108288.

Grylls, T., van Reeuwijk, M., 2022. How trees affect urban air quality: It depends on the source. Atmos. Environ. 290, 119275.

Guan, D., Zhang, Y., Zhu, T., 2003. A wind-tunnel study of windbreak drag. Agricult. Forest. Meterol. 118, 75–84.

Ikegaya, N., Okaze, T., Kikumoto, H., Imano, M., Ono, H., Tominaga, Y., 2019. Effect of the numerical viscosity on reproduction of mean and turbulent flow fields in the case of a 1: 1: 2 single block model. J. Wind Eng. Ind. Aerodyn. 191, 279–296.

Irwin, H., 1981. The design of spires for wind simulation. J. Wind Eng. Ind. Aerodyn. 7, 361–366. http://dx.doi.org/10.1016/0167-6105(81)90058-1.

Janhäll, S., 2015. Review on urban vegetation and particle air pollution–deposition and dispersion. Atmos. Environ. 105, 130–137.

Jeanjean, A.P., Buccolieri, R., Eddy, J., Monks, P.S., Leigh, R.J., 2017. Air quality affected by trees in real street canyons: The case of marylebone neighbourhood in central london. Urban For. Urban Green. 22, 41–53.

Jeanjean, A.P., Hinchliffe, G., McMullan, W., Monks, P.S., Leigh, R.J., 2015. A cfd study on the effectiveness of trees to disperse road traffic emissions at a city scale. Atmos. Environ. 120, 1–14.

Jiao, H., Takemi, T., 2024. Investigating the influence of stepped roofs on wind dynamics using large eddy simulation. Build. Environ. 262, 111819.

Jiao, H., Takemi, T., 2025. Using large eddy simulation to investigate pollutant dispersion over stepped roofs. Build. Environ. 274, 112704.

Kellnerová, R., Fuka, V., Uruba, V., Jurčáková, K., Nosek, Š., Chaloupecká, H., Jaňour, Z., 2018. On street-canyon flow dynamics: Advanced validation of les by time-resolved piv. Atmosphere 9, 161.

Kim, Y., Wu, Y., Seigneur, C., Roustan, Y., 2018. Multi-scale modeling of urban air pollution: development and application of a street-in-grid model (v1. 0) by coupling munich (v1. 0) and polair3d (v1. 8.1). Geosci. Model. Dev. 11, 611–629.

Lim, H., Hertwig, D., Grylls, T., Grimmond, S., van Reeuwijk, M., 2022. Pollutant dispersion by tall buildings: laboratory experiments and large-eddy simulation. Exp. Fluids 63, 92.

Lim, H.C., Thomas, T., Castro, I.P., 2009. Flow around a cube in a turbulent boundary layer: Les and experiment. J. Wind Eng. Ind. Aerodyn. 97, 96–109.

Llaguno-Munitxa, M., Bou-Zeid, E., Hultmark, M., 2017. The influence of building geometry on street canyon air flow: Validation of large eddy simulations against wind tunnel experiments. J. Wind Eng. Ind. Aerodyn. 165, 115–130.

Maison, A., Lugon, L., Park, S.J., Boissard, C., Faucheux, A., Gros, V., Kalalian, C., Kim, Y., Leymarie, J., Petit, J.E., et al., 2024. Contrasting effects of urban trees on air quality: From the aerodynamic effects in streets to impacts of biogenic emissions in cities. Sci. Total Environ. 946, 174116.

Majumdar, D., Vita, G., Ramponi, R., Glover, N., van Reeuwijk, M., 2025. The drag length is key to quantifying tree canopy drag. J. Wind Eng. Ind. Aerodyn. 261, 106084.

Manickathan, L., Defraeye, T., Allegrini, J., Derome, D., Carmeliet, J., 2018. Comparative study of flow field and drag coefficient of model and small natural trees in a wind tunnel. Urban For. Urban Green. 35, 230–239.

Marro, M., Gamel, H., Méjean, P., Correia, H., Soulhac, L., Salizzoni, P., 2020. High-frequency simultaneous measurements of velocity and concentration within turbulent flows in wind-tunnel experiments. Exp. Fluids 61, 1–13.

Marucci, D., Carpentieri, M., 2019. Effect of local and upwind stratification on flow and dispersion inside and above a bi-dimensional street canyon. Build. Environ. 156, 74–88.

Merlier, L., Jacob, J., Sagaut, P., 2018. Lattice-Boltzmann large-eddy simulation of pollutant dispersion in street canyons including tree planting effects. Atmos. Environ. 195, 89–103.

Mishra, A., Bi, D., Carpentieri, M., Barlow, J., Robins, A., Placidi, M., 2025. Tall building clusters in urban canopies: An experimental analysis of wake and dispersion characteristics. Int. J. Heat Fluid Flow 116, 109960.

Moonen, P., Gromke, C., Dorer, V., 2013. Performance assessment of large eddy simulation (les) for modeling dispersion in an urban street canyon with tree planting. Atmos. Environ. 75, 66–76.

Nakajima, K., Ooka, R., Kikumoto, H., 2018. Evaluation of k-ε reynolds stress modeling in an idealized urban canyon using les. J. Wind Eng. Ind. Aerodyn. 175, 213–228.

Nazarian, N., Krayenhoff, E.S., Martilli, A., 2020. A one-dimensional model of turbulent flow through urban canopies (mlucm v2. 0): updates based on large-eddy simulation. Geosci. Model. Dev. 13, 937–953.

Oke, T.R., 1988. Street design and urban canopy layer climate. Energy Build. 11, 103–113.

Oke, T.R., Mills, G., Christen, A., Voogt, J.A., 2017. Urban Climates. Cambridge University Press.

Owens, S.O., Majumdar, D., Wilson, C.E., Bartholomew, P., van Reeuwijk, M., 2024. A conservative immersed boundary method for the multi-physics urban large-eddy simulation model udales v2. 0. EGUsphere 2024, 1–33.

Peng, Y., Buccolieri, R., Gao, Z., Ding, W., 2020. Indices employed for the assessment of urban outdoor ventilation-a review. Atmos. Environ. 223, 117211.

Perret, L., Basley, J., Mathis, R., Piquet, T., 2019. The atmospheric boundary layer over urban-like terrain: influence of the plan density on roughness sublayer dynamics. Bound.-Layer Meteorol. 170, 205–234.

Perret, L., Savory, E., 2013. Large-scale structures over a single street canyon immersed in an urban-type boundary layer. Bound.-Layer Meteorol. 148, 111–131.

Pope, S.B., 2000. Turbulent Flows. Cambridge University Press.

Resler, J., Eben, K., Geletič, J., Krč, P., Roseckỳ, M., Sühring, M., Belda, M., Fuka, V., Halenka, T., Huszár, P., et al., 2021. Validation of the palm model system 6.0 in a real urban environment: a case study in dejvice, prague, the czech republic. Geosci. Model. Dev. 14, 4797–4842.

Revelli, R., Porporato, A., 2018. Ecohydrological model for the quantification of ecosystem services provided by urban street trees. Urban Ecosyst. 21, 489–504.

Reynolds, R., Castro, I., 2008. Measurements in an urban-type boundary layer. Exp. Fluids 45, 141–156.

Reynolds, R., Hayden, P., Castro, I., Robins, A., 2007. Spanwise variations in nominally two-dimensional rough-wall boundary layers. Exp. Fluids 42, 311–320.

Salim, S.M., Cheah, S.C., Chan, A., 2011. Numerical simulation of dispersion in urban street canyons with avenue-like tree plantings: comparison between rans and les. Build. Environ. 46, 1735–1746.

Salizzoni, P., Marro, M., Soulhac, L., Grosjean, N., Perkins, R.J., 2011. Turbulent transfer between street canyons and the overlying atmospheric boundary layer. Bound.-Layer Meteorol. 141, 393–414.

Salizzoni, P., Soulhac, L., Mejean, P., 2009. Street canyon ventilation and atmospheric turbulence. Atmos. Environ. 43, 5056–5067.

Salizzoni, P., Soulhac, L., Mejean, P., Perkins, R.J., 2008. Influence of a two-scale surface roughness on a neutral turbulent boundary layer. Bound.-Layer Meteorol. 127, 97–110.

Santiago, J.L., Martilli, A., Martin, F., 2017. On dry deposition modelling of atmospheric pollutants on vegetation at the microscale: Application to the impact of street vegetation on air quality. Bound.-Layer Meteorol. 162, 451–474.

Shu, C., Wang, L.L., Mortezazadeh, M., 2020. Dimensional analysis of reynolds independence and regional critical reynolds numbers for urban aerodynamics. J. Wind Eng. Ind. Aerodyn. 203, 104232.

Soulhac, L., Salizzoni, P., Cierco, F.X., Perkins, R., 2011. The model SIRANE for atmospheric urban pollutant dispersion; part I, presentation of the model. Atmos. Environ. 45, 7379–7395.

Soulhac, L., Salizzoni, P., Mejean, P., Perkins, R., 2013. Parametric laws to model urban pollutant dispersion with a street network approach. Atmos. Environ. 67, 229–241.

Stoll, R., Gibbs, J.A., Salesky, S.T., Anderson, W., Calaf, M., 2020. Large-eddy simulation of the atmospheric boundary layer. Bound.-Layer Meteorol. 177, 541–581.

Suter, I., Grylls, T., Sützl, B.S., Owens, S.O., Wilson, C.E., van Reeuwijk, M., 2022. udales 1.0: a large-eddy simulation model for urban environments. Geosci. Model. Dev. 15, 5309–5335.

Suter, I., Grylls, T., Sützl, B., van Reeuwijk, M., 2021. udales 1.0. 0: a large-eddy-simulation model for urban environments. Geosci. Model. Dev. Discuss. 2021, 1–40.

Teng, M., Duró Diaz, J.M., Mestres, E., Muela Castro, J., Lehmkuhl, O., Rodriguez, I., 2025. Atmospheric boundary layer over urban roughness: Validation of large-eddy simulation. Phys. Fluids 37.

Vanderwel, C., Ganapathisubramani, B., 2015. Effects of spanwise spacing on large-scale secondary flows in rough-wall turbulent boundary layers. J. Fluid Mech. 774, R2.

Vardoulakis, S., Fisher, B.E., Pericleous, K., Gonzalez-Flesca, N., 2003. Modelling air quality in street canyons: a review. Atmos. Environ. 37, 155–182.

Vreman, A., 2004. An eddy-viscosity subgrid-scale model for turbulent shear flow: Algebraic theory and applications. Phys. Fluids 16, 3670–3681.

Wang, W., Cao, Y., Okaze, T., 2021. Comparison of hexahedral, tetrahedral and polyhedral cells for reproducing the wind field around an isolated building by les. Build. Environ. 195, 107717.

Xie, Z., Castro, I.P., 2006. Les and rans for turbulent flow over arrays of wall-mounted obstacles. Flow Turbul. Combust. 76, 291–312.

Xie, Z., Voke, P.R., Hayden, P., Robins, A.G., 2004. Large-eddy simulation of turbulent flow over a rough surface. Bound.-Layer Meteorol. 111, 417–440.

Zheng, X., Montazeri, H., Blocken, B., 2021. Large-eddy simulation of pollutant dispersion in generic urban street canyons: Guidelines for domain size. J. Wind Eng. Ind. Aerodyn. 211, 104527.

Zhu, Z., Kleinn, C., Nölke, N., 2021. Assessing tree crown volume—a review. For.: An Int. J. For. Res. 94, 18–35.